DEVELOPMENT OF ROOM TEMPERATURE H_2S GAS SENSORS USING FLOWER-LIKE ZnO NANORODS

by

Sara Ghaderahmadi

B.Sc, in Electrical Engineering, K.N.Toosi University of Technology, Iran, 2020

A THESIS SUBMITTED IN PARTIAL FULFILLMENT OF

THE REQUIREMENTS FOR THE DEGREE OF

MASTER OF APPLIED SCIENCE

in

THE COLLEGE OF GRADUATE STUDIES

(Electrical Engineering)

THE UNIVERSITY OF BRITISH COLUMBIA

(Okanagan)

December 2021

The following individuals certify that they have read, and recommend to the College of Graduate Studies for acceptance, the thesis entitled:

DEVELOPMENT OF ROOM TEMPERATURE H_2S GAS SENSOR USING FLOWER-LIKE ZnO NANORODS

submitted by Sara Ghaderahmadi in partial fulfillment of the requirements for

the degree of Master of Applied Science

Examining Committee:

Dr. Mina Hoorfar, School of Engineering
Supervisor

Dr. Mohammad Arjmand, School of Engineering
Co-supervisor

Dr. Jian Liu, School of Engineering
Supervisory Committee Member

Dr. Anas Chaaban, School of Engineering
Supervisory Committee Member

Dr. Sumi Siddiqua, School of Engineering
University Examiner

Abstract

Detection of toxic gases such as hydrogen sulfide (H_2S) at low temperatures is of high importance as it reduces power consumption, increases long-term stability, and lowers the danger of explosion in the presence of flammable gases. Among different gas sensors, chemiresistive metal oxide semi-conductor sensors are the most popular type due to their low cost, high sensitivity, compact size, ease of use, and high thermal and mechanical stability. However, these sensors generally require a high operating temperature (>100℃), attributed to their insufficient surface area. Hence, their pristine bulk structures cannot meet the requirements of low-temperature gas sensing. To overcome these limitations, the bulk structure of metal oxide sensors can be modified geometrically for an increased surface area. Herein, we fabricated flower-like ZnO nanorods using a modified hydrothermal method in two different grain sizes of 19 and 23nm. The sample was tested toward H_2S and a range of volatile organic compounds. The sample with smaller grain size provided 7.4 as response value as well as fast response and recovery time of 293 and 186s, respectively, toward 100ppm H_2S at room temperature. The results indicate the potential of the sensing layer for real-time monitoring and detection of hazardous gases detection at room temperature.

Lay Summary

Hydrogen sulfide (H_2S) is a highly flammable and toxic gas with a fast active poison. The health hazards upon exposure to this gas is highly dependent on the exposure duration and concentration. Thus, a highly sensitive and fast gas sensor is required for safe and effective detection of H_2S, especially at workspace. In this study, we have chosen ZnO as the sensing layer due to its ease of fabrication, low cost, non-toxicity, and thermal and mechanical stability. The fabricated ZnO nanostructures showed promising gas sensing properties, including high response value, fast response and recovery time, and acceptable short-term and long-term stability at room temperature.

Preface

All chapters in the thesis are based on the work conducted at the University of British Columbia in Advanced Thermofluidics Laboratory (ATFL) and Nanomaterials and Polymer Nanocomposites Laboratory (NPNL) by Sara Ghaderahmadi under the supervision of Dr. Mina Hoorfar and Dr. Mohammad Arjmand. During the whole experiments in the thesis, I was responsible for all the samples preparation, gas sensing tests, and data analysis. My supervisors, Dr. Mina Hoorfar and Dr. Mohammad Arjmand, and the committee member guided and led me through the journey of accomplishing this initiative..

A version of chapter two has been published as the following paper: Sara Ghaderahmadi, Milad Kamkar, Nishat Tasnim, Mohmmad Arjmand, Mina Hoorfar. A Review of Low-temperature H_2S Gas Sensors: Fabrication and Mechanism. New Journal of Chemistry, 10.1039/D1NJ02468J.

Table of Contents

List of Tables

List of Figures

List of Abbreviations

MOS	Metal oxide semi-conductor
OSHA	Occupational safety and health administration
SAW	Surface acoustic wave
SEM	Scanning Electron Microscopy
VOC	Volatile Organic Compound
XPS	X-Ray Photoelectron Spectroscopy
XRD	X-Ray Diffraction

Acknowledgements

I would like to express my highest gratitude to my supervisors Dr. Mina Hoorfar and Dr. Mohammad Arjmand who believed in me and gave me the opportunity to work in their research groups. Your continuous support and guidance encouraged me to pursue my research path. It was a great honor to work under your supervision.

I would also like to thank all my lab mates in Advanced Thermofluidics Laboratory (ATFL) and Nanomaterials and Polymer Nanocomposites Laboratory (NPNL) for all their guidance and motivation.

Above all, my deepest appreciation belongs to my caring and supportive family. Your support has always helped me survive all the challenges and difficulties throughout my life.

Dedication

To all international students who leave everything behind in the pursuit of a brighter future.

Chapter 1: Introduction

1.1 General background

The increasing demand for monitoring and detecting flammable and toxic gases has resulted in extensive attention on gas sensor development. Gas sensors have a wide range of applications from domestic to industrial. They can be used as breath analyzers to detect diseases such as diabetes at an early stage [1, 2]. They are also used to monitor the environment quantitatively and qualitatively, in houses to detect the level of CO [3, 4], and in major industries such as natural gas petrochemical complexes [5, 6], to detect the level of hazardous gas to avoid potential health hazards. Hydrogen sulfide (H_2S) is among the most hazardous and toxic gases. Also known as swage gas, H_2S is the second most toxic gas existing in the workplace after carbon monoxide (CO), according to Occupational Safety and Health Administration (OSHA) [7]. The poisonous effect of H_2S upon exposure is highly dependent on its concentration and the length of exposure. Therefore, the effects include headache, nausea, skin and eye irritation, and even death, which can be caused due to >100ppm exposure to H_2S. OSHA has developed regulations for workplace H_2S exposure limits, including an 8hr exposure time limit to 10ppm and 15min exposure time limit to 15ppm.

Among different mechanisms employed for H_2S detection, metal-oxide-semiconductor (MOS)-based sensors have emerged to be the most favorable candidate. MOS sensors are low cost, easy to fabricate, stable in the long term, and highly sensitive [8]. They are fabricated in different geometries ranging from bulk materials to nanostructures and are easily tuned physically and chemically to meet each specific application demand. However, they usually operate at high-temperature ranges, which increases the power consumption and reduces the long-term stability. A low operating temperature in conjunction with high sensitivity and rapid response/recovery kinetics is required for safe and effective sensing of flammable and explosive gases such as H_2S

to prevent operational and health hazards during in situ monitoring. To overcome the high operating temperature, the bulk structure of metal oxide sensors should be modified either geometrically or chemically for an increased surface area. Therefore, great efforts have been made to fabricate non-spherical micro-nano structures, such as nanofibers [9, 10], nanosheets [11, 12], nanowire [13, 14], nanotubes [15, 16], microspheres [17], and nanorods [18, 19], for detecting different hazardous gases.

1.2 Thesis objectives

In this M.Sc. thesis, we have developed a room temperature flower-like ZnO-based gas sensor. We have investigated the gas sensing properties of the ZnO nanorods upon exposure to H_2S, as well as a range of VOCs. Moreover, we have investigated the effect of grain size on gas sensing mechanisms by comparing the gas sensing properties of two samples of ZnO nanorods in different grain sizes. This research draws a roadmap for optimization of the gas sensing performance of the MOS nanostructure toward different target gases.

Chapter 1 is a brief introduction to gas sensors, objectives, and structure of this M.Sc. thesis. Chapter 2 is a comprehensive literature review on low-temperature H_2S gas sensors using different metal-oxides and their physical modification for enhanced gas sensing properties, including reduced operating temperature. Chapter 3 covers the methodology and experimental procedures used for this study, including synthesis method, characterization techniques, and gas sensor response analysis, as well as the gas sensing setup. Chapter 4 is devoted to results and discussion in which the flower-like ZnO nanostructure chemical structure and gas sensing properties are investigated in detail. First, the structural and chemical properties of the flower-like ZnO nanorods are determined using different characterization techniques. Then, the ZnO nanorods are tested toward H_2S and a range of VOCs to investigate their potential in room-temperature gas sensing. Finally, we have investigated the effect of grain size on gas sensing

properties. Lastly, Chapter 5 summarizes the achievements of the current work and our suggestions toward potential future studies.

Chapter 2: Literature review

This chapter aims to review the literature on low-temperature H_2S gas sensing by investigating a wide range of metal oxides and the main mechanisms in reducing the operating temperature down to room temperature. As the thesis is focused on room-temperature ZnO-based gas sensing, the literature review includes describing the gas sensing mechanism of metal oxide semi-conductors and investigating the most favorable metal-oxides for low-temperature H_2S gas sensing (i.e., ZnO, CuO, In_2O_3, and WO_3) and the dominant mechanisms on reducing the operating temperature.

2.1 Hydrogen sulfide (H_2S)

Hydrogen sulfide (H_2S) gas sensing is of particular concern due to its pollutant toxic and corrosive nature. Also known as sewer gas, H_2S is a highly contaminant toxic gas with a fast-acting poison [20]. It is a colorless gas with a malodorous rotten-egg smell, even at very low levels of 0.5 parts per billion (ppb) in air. Amon its hazardous characteristics, it is corrosive, flammable, and explosive at 4.3 to 45%vol in air.

H_2S is produced from both natural- and human-based sources. This gas can be naturally produced from the bacterial breakdown of sulfate in anaerobic environments, which is one of the key components in the sulfur cycle [21] (see Figure 2.1). The sulfate can be produced from different industrial resources or it can be a result of the degradation of sulfur-containing proteins in mammals [22]. Some of the significant sources of H_2S include petroleum, natural gas, volcanic gas, hot spring, and human and animal wastes [7, 23].

In recent years, human-based sources of H_2S concentration and emission in the air have gained greater attention compared with natural sources. H_2S can be anthropogenically produced as a by-product of various industrial processes such as petroleum and natural gas extraction and purification, paper and pulp manufacturing, textile production, chemical manufacturing,

wastewater treatment, and food processing [24]. The amount of the emitted H_2S from these human-based sources is hard to be quantified due to the lack of comprehensive reports. However, studies have shown that the main source of H_2S emission in western Canada is the oil and gas industry.

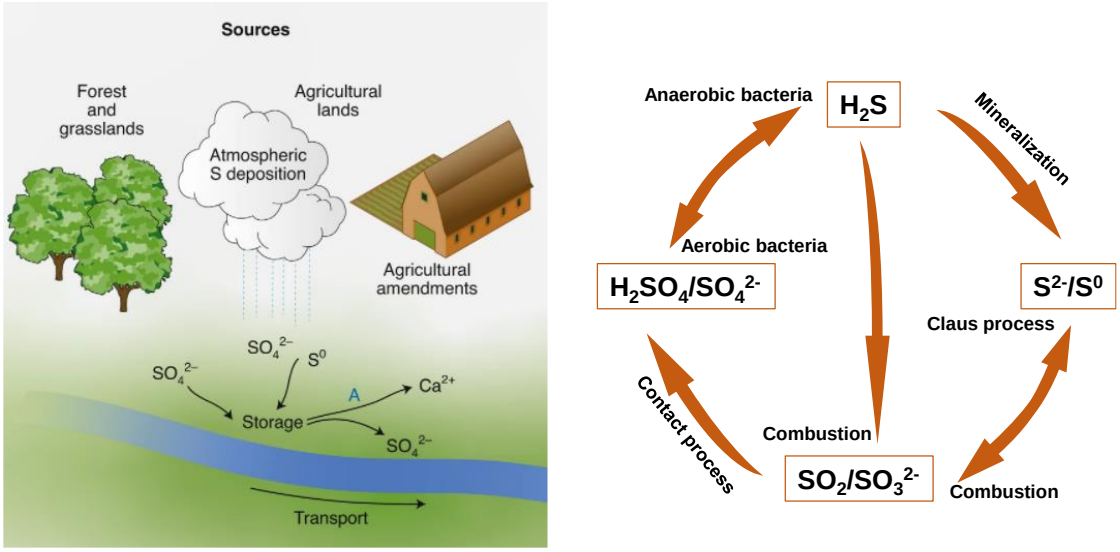

Figure 2.1 Participation of H_2S in the global sulfur cycle. Reproduced from ref. [25]. Copyright © 2020 Natures.

H_2S gas is also heavier than air and can be collected in low-lying and enclosed areas at or below ground level, making these confined spaces hazardous for work. According to the Occupational Safety and Health Administration (OSHA), H_2S is the second most toxic gas existing in the workplace after carbon monoxide (CO). The poisonous effect of H_2S upon exposure is highly dependent on its concentration, and it can be categorized into three groups, including 1) acute exposure, > 300ppm, 2) post-acute exposure, >100ppm, and 3) chronic exposure, <1ppm (see Figure 2.2) [26]. Acute exposure causes collapse, unconsciousness, and death, which happens due to cardiopulmonary paralysis. Post-acute exposure occurs upon exposure to lower concentrations over a long period of time, i.e., 30 minutes, which causes difficulty in breathing, coma, and even death [27]. Chronic exposure results from exposure to less than 1ppm of H_2S gas over several days; the side effects include nausea, headache, and skin and eye irritation [27].

Full detail of health hazards upon exposure to different concentrations of H_2S is listed in Table 2.1. OSHA has developed regulations for workplace H_2S exposure limits, including an 8hr exposure time limit to 10ppm and 15min exposure time limit to 15ppm.

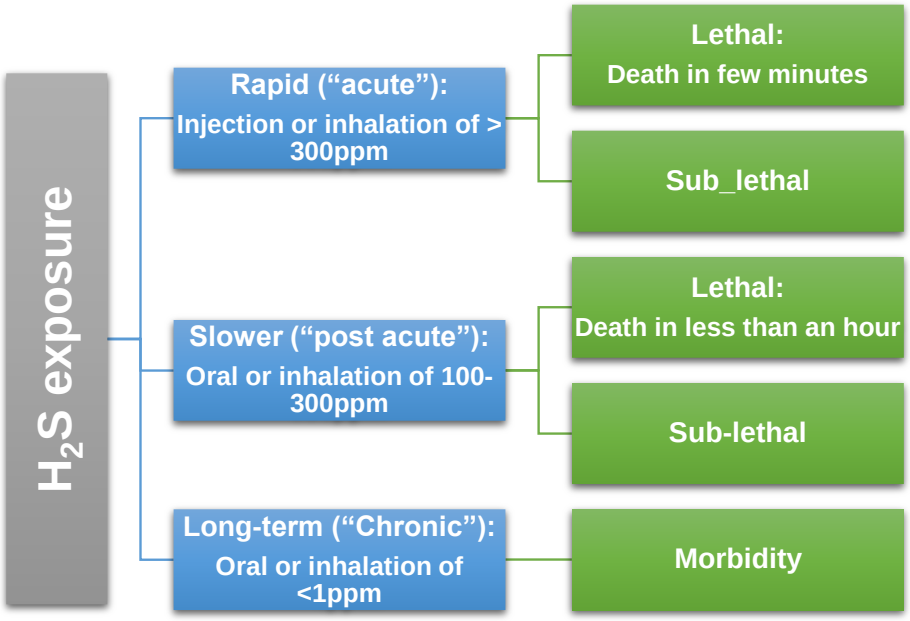

Figure 2.2 List of lethal and sub-lethal H_2S poisoning.

Table 2.1 List of physical hazards of H_2S upon exposure to different concentrations [28].

H_2S concentration (ppm)	Effect
0-10	Threshold for eye, nose, and throat irritation
10-50	Headache, dizziness, nausea, vomiting, coughing, difficulty breathing
50-100	Serious eye damage
150-250	Loss of olfactory sense
320-500	Pulmonary edema with risk of death
500-700	Collapse in five minutes, serious eye damage
700-1000	Rapid unconsciousness, collapse after 1 or 2 breaths
1000-2000	Immediate collapse with paralysis of respiration, death in few minutes

Hydrogen sulfide has some major industrial applications as well. One of its most important applications is on producing sulfur and then sulfuric acid via Claus process and contact process, respectively. Sulfuric acid is one of the most traded chemicals in the world and it is used in phosphate and other fertilizers production. The Claus process is briefly shown in Figure 2.3. Some other applications of H_2S include dye and pesticide production.

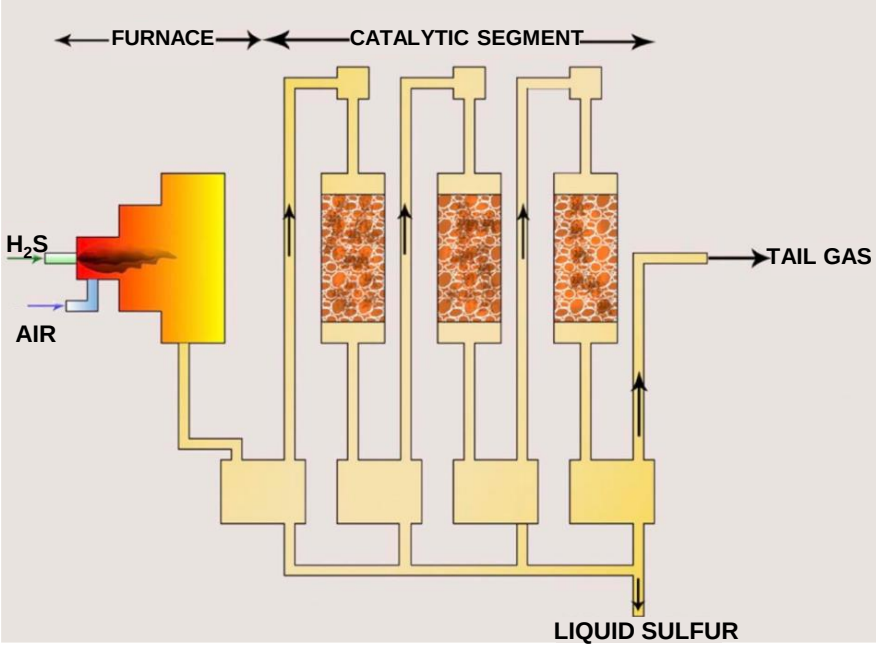

Figure 2.3 Schematic of the process of producing sulfur from H_2S known as Claus process. Reproduced from ref. [29]. Copyright © 2016 Elsevier.

2.2 H_2S gas sensing

It is now well established in the previous section that H_2S gas sensors are a significantly important component in environmental and industrial applications. Due to its wide range of sources and applications both in nature and industry several efforts have been done in the literature to develop efficient H_2S gas sensors. There are different mechanisms employed to

detect H_2S, including surface acoustic wave (SAW) [30], optical [31], and chemiresistive [8], which are briefly explained in the following section:

Surface acoustic wave (SAW): Surface acoustic wave gas sensors work based on the changes in the boundary conditions of the propagating wave, which is caused as a result of the interaction between the sensing layer and the target gas. The sensing layer is fabricated on a piezoelectric substrate, where the surface acoustic wave is excited. As the sensing layer is exposed to a target gas, the velocity and/or amplitude of the wave changes. The changes are converted to electric signals for further analysis [32].

The sensing setup consists of two interdigitated transducers (IDTs) (e.g., gold and aluminum), a piezoelectric substrate (e.g., quartz, $LiNbO_3$, and silicon), and a sensing layer. The mechanical input signal is converted to an electric signal via the input IDT and converted back to a mechanical signal at the output IDT, using the piezoelectric effect. A simplified schematic of a SAW gas sensor is shown in Figure 2.4. These sensing devices are usually the size of a few millimeters. Their compact size incorporated with great stability in harsh environments, high speed with real-time wireless monitoring has made SAW sensors an ideal candidate for bio-implanted applications. However, SAW-based sensing layers suffer from poor selectivity and fabrication complexity due to their small size [33].

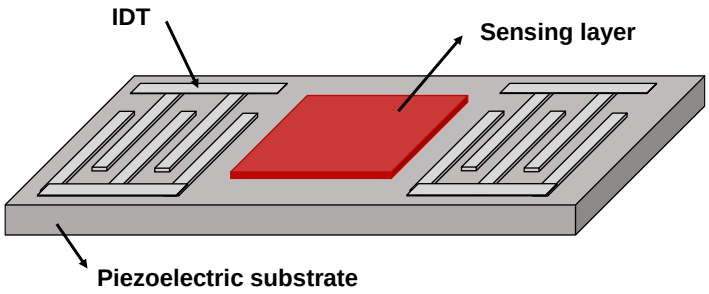

Figure 2.4 Schematic of SAW gas sensor.

Optical: Optical gas sensors have recently attracted significant attention due to their properties such as down to room operating temperature, high selectivity, ppb level of detection,

and real-time monitoring [34]. These types of gas sensors work based on the adsorption properties of different chemical species of different regions of electromagnetic spectra [35]. The adsorption spectra are specific for each chemical species, therefore optical gas sensors can provide high selectivity. The adsorption happens at different regions of the electromagnetic spectra: UV (200-400nm), near IR (700nm-2.5μm), and mid-IR (2.5-14μm). The adsorption near mid-IR happens because of molecular vibration and rotation. Therefore, the adsorption bands can be significantly weak which would require high quality and expensive source and detectors and lengthy path sensing setups. As a result, cost, complexity, and space have limited their application as commercial gas sensors in the industry.

Recently, a miniaturized type of optical gas sensor has been introduced for possible environmental monitoring applications, called fiber-optic [36]. A simple schematic of a fiber-optic gas sensor is shown in Figure 2.5. The optical fiber is partially exposed to the sensing membrane. As a result of the reaction between the white light passing through the fiber optic and the sensing membrane, some of its physical and chemical characteristics such as refractive index changes, which is monitored in the detector [33]. The fiber-optic gas sensors can provide high sensitivity, selectivity, and stability; however, their fabrication process is complex due to the significantly small size of the optical fiber [37, 38].

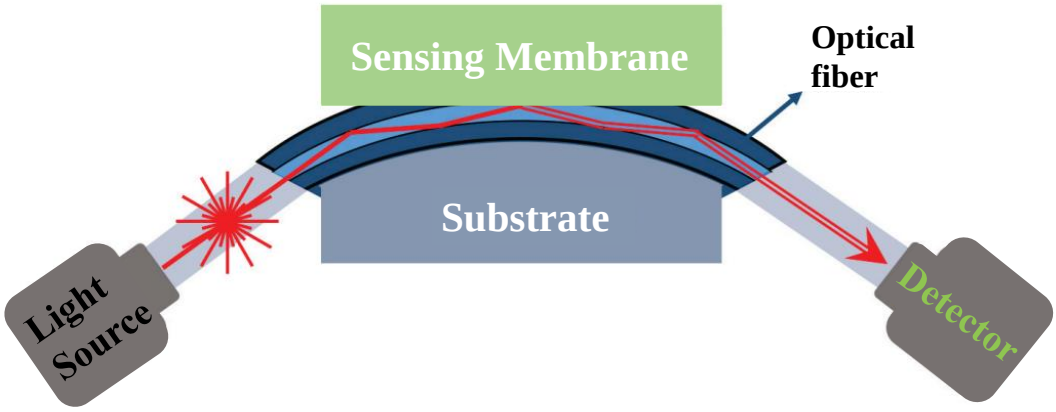

Figure 2.5 Schematic of a fiber optic gas sensing setup. Reproduced from ref. [33]. Copyright © Sensors 2019.

Chemiresistive: Among the aforementioned mechanisms, chemiresistive-based metal oxide semi-conductor (MOS) sensing layers are the most promising gas sensors due to great properties such as low cost, ease of fabrication, high thermal and mechanical stability, and high sensitivity [39]. MOS sensing layers are fabricated in different geometries from bulk to nanostructures (e.g., nanorods [40], nanowires [41], nanosheets [20], and nanofibers [9]) with a wide range of operating temperatures.

Briefly, chemiresistive gas sensors work based on the electrical conductivity change in the presence of the target gas. The extent of the change in conductivity depends on the gas type and concentration. In these types of sensors, the sensing layer directly interacts with the target gas, resulting in an alternation of the physical and chemical properties of the sensing layer. In essence, oxygen is chemisorbed on the surface of the sensing layer in the form of O_2^x. As reported in the literature, the chemisorbed oxygen at room temperature is in the form of O_2^- (see Equation (1)) [42]. This oxygen species acts as a surface acceptor, trapping free electrons from the conduction band, forming an electron-depleted surface layer. As the material is exposed to a reducing gas such as H_2S, free electrons are released based on Equation (2). The released electron changes

the sensing layer conductivity, which causes an increase or decrease in n-type (a type of semiconductor where the majority of charge carriers are electrons) and p-type (a type of semiconductor where the majority of charge carriers are holes) materials, respectively.

$$O_{2(atmosophere)} + e^-_{(metal\ oxide\ surface)} \rightarrow O^-_{2(ads)} \quad (2.1)$$

$$2H_2S_{(ads)} + 3O^-_{2(ads)} \rightarrow 2SO_2 + 2H_2O + 3e^- \quad (2.2)$$

Gas sensors are characterized based on six criteria: (1) response value, (2) response time, (3) recovery time, (4) stability, (5) reproducibility, and (6) selectivity. The first three criteria can be obtained from one dynamic cycle, defined as a sensor being exposed to a specific concentration of a target gas for a period of time during which the monitored parameters reach either a peak or a minimum and then is exposed to ambient air to recover to the baseline value (i.e., the steady-state resistance of the sensor in the air). Based on the measurement setup, the monitored parameters can be resistance, conductivity, current, or voltage. Response and recovery times are defined as the time where the response reaches 90% of the total change upon exposure to a target gas and air, respectively (see Figure 2.6) [43]. A response value can be defined in two different ways: (i) the ratio of the total change over the pristine value of the measured parameter, which in this case, it is usually reported in percentage ($\Delta R/R_a$), or (ii) the ratio of either the base-line over the peak magnitude and vice versa in *n*-type (R_a/R_g) and *p*-type (R_g/R_a) materials, respectively. To evaluate the selectivity of a gas sensor, the sensor is either exposed to a mixture of gases (including the target gas) or is exposed individually to different interfering gases at certain concentrations. The selectivity is examined based on the response value to the target gas compared to the response value to interfering gases. The larger the difference, the higher the selectivity of the sensor.

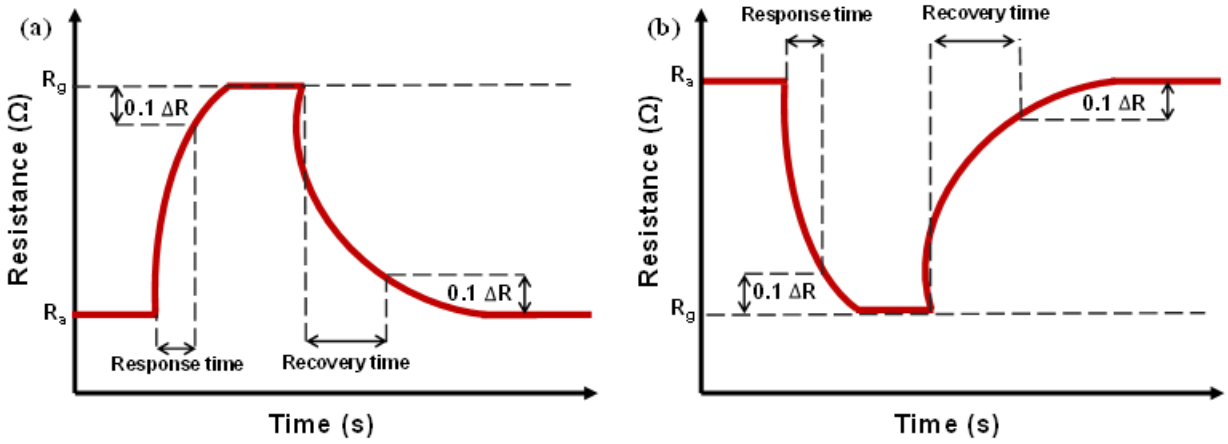

Figure 2.6 The definition of response time and recovery time toward a reducing gas in (a) n-type and (b) p-type semi-conductor.

2.3 Low-temperature H_2S gas sensing

In addition to the mentioned criteria to characterize a sensing layer in section 2.2, there is another important property which is the operating temperature. The vital role of metal oxides in the fabrication of H_2S gas sensors seems to be indispensable due to their sensitivity, mechanical and thermal stability, and easy fabrication. However, they usually operate at high temperatures, i.e., >150℃ which has some significant drawbacks including decreased long-term stability and increased power consumption. Therefore, several efforts have been done in the literature to decrease the operating temperature down to room temperature.

To date, only a few metal oxides have been applied for low-temperature H_2S gas sensing. However, this challenge can be addressed by an emergent body of research centered around the modification of the MOS sensing layers via both physical (e.g., geometry and size) and chemical (e.g., doping) modifications. In the case of physical modification, as the structure sizes decrease from micro- to the nanoscale, the specific area increases dramatically, thereby increasing the active sites in nanostructures for oxygen adsorption. Although this might increase the baseline resistance, the sensor will demonstrate higher sensitivity to target analytes due to the larger

number of electrons being trapped in the depletion layer [44]. Chemical modification is the second method to improve gas sensing properties for decreased operating temperature. The main approaches for chemical modifications are the incorporation of noble metals as modifiers [45] or the use of hybrid metal oxide semi-conductors [46]. There are also other emergent approaches, such as the use of highly conductive nanoparticles [47].

Although the main focus of this thesis is on the physical modification method, we have provided an overview of different types of MOS (including ZnO, CuO, In_2O_3, and WO_3) reported for low-temperature gas sensing of H_2S with a comprehensive evaluation of their physical and chemical modification for enhanced sensing performance at low operating temperature.

2.3.1 ZnO

ZnO, with a wide bandgap of 3.37 eV, is a multifunctional semiconductor material [48]. Promising gas sensing and piezoelectric properties, as well as nontoxicity, ease of fabrication, and high thermal and chemical stability have rendered ZnO a multifunctional material. As a result, ZnO has been used in a wide range of applications, from piezoelectric nanogenerators [49], UV sensors [50], solar cells [51] to gas sensors [52]. As for the latter, ZnO has been widely used in H_2S gas sensing applications in different geometries and structures such as thin films [53], nanosheets [54], nanoparticles, nanorods [44, 55], and nanofibers (summarized in Table 2.2). ZnO interaction with H_2S can be described as follows:

$$ZnO + 2H_2S_{(ads)} \rightarrow ZnS + H_2O \qquad (2.3)$$

Nimbalkar et al. [53] studied the performance of a ZnO-based thin film H_2S gas sensor. The thin film was synthesized using a sol-gel spin-coating technique. The precursor solution was made via dissolving zinc acetate in ethanol. After stirring, the solution was spin-coated on a glass substrate, followed by air-drying and then, annealing at 600℃ for 60min to obtain a thin film with a thickness of 34nm. Further analytical investigation methods such as field emission scanning electron microscopy (FESEM) showed that the thin film was composed of spherical ZnO

nanoparticles (referred to as 0D) placed closely by each other, forming a porous crystalline structure with an average size of 37nm [53]. Although the sensor had a high operating temperature of 300℃ with a relatively low response of 3.25 (R_a/R_g) at 100ppm, it showed fast response and recovery times of 10 and 200s, respectively. The rationale behind the long recovery time compared to the response time was that the gas desorption phenomenon is normally a slow process in nature [53].

Changing the geometry of the particles from 0D (spherical) to 1D (nanorod or nanotube) and 2D (nanosheet) improves the gas sensing properties and decreases the operating temperature. This improvement is the result of an increase in the effective surface area. In this regard, various geometries with different specific areas, affecting gas molecule adsorption and desorption, have been reported in the literature [56, 57]. For instance, ZnO has been used in the form of nanorod [55], porous nanorod, [44], and dendritic structure [58] for H_2S low-temperature gas sensing.

Shinde et al. [55] reported a ZnO nanorod sensor synthesized using the spray pyrolysis method operable at low temperatures. As it can be seen in Figure 2.7a, the hexagonal wurtzite ZnO nanorods were fabricated with sizes ranging from 20 to 80nm. Although the sensor showed a response of 30 (R_a/R_g) at 35℃, the highest response was obtained at 50℃ with an excellent magnitude of 61.7 upon exposure to 100ppm of the target gas (see Figure 2.7b). Additionally, the response magnitude increased as the gas concentration rose, as expected. At the optimum operating temperature (i.e., 50 ℃), the sensor showed a significant fast response time of 4s and a short recovery time of the 60s, shown in Figure 2.7c. The fast response may be associated with a 1D nanostructure, featuring an extremely large specific area [55].

Porous structures are another effective feature used for improving the gas sensing-related parameters, including electrical conductivity, catalytic activity, and adsorption-desorption rate

[44]. More importantly, the increased specific area achieved by porous structures provides a large number of active sites for oxygen adsorption. As an example, Hosseini et al. [44] reported a room temperature H_2S gas sensor based on porous ZnO nanorods forming a flower-like structure. The sensing layer was fabricated by heating ZnO and graphite powder in a horizontal tube furnace. The fabricated porous nanorods were 300-500nm in diameter and 7-9.5μm in length (see Figure 2.7d). It was shown that the synthesized aggregated flower-like ZnO nanorods, due to their porous nature, had a large specific area [44]. As it is shown in Figure 2.7e, the sensor was sensitive at room temperature with response magnitudes as high as 296 and 581 ($^{R_a}/_{R_g}$) upon exposure to 1 and 5ppm H_2S, respectively. Interestingly, the study reported that the sensor response decreased with the temperature elevation and attributed this to two factors: (1) the increase in charge carriers due to larger inter-gaps being ionized below the conduction band, and (2) facilitation of phonon-assisted tunneling [44]. The latter can cause a decrease in the resistance of ZnO as an *n*-type semiconductor. As a result, the response dramatically decreased to 2.4 and 3.7 for 1 and 5ppm H_2S at 250℃, respectively. The obtained response time and recovery time were 320 and 3592s at room temperature, respectively. However, at elevated temperatures, decomposition, adsorption, and desorption processes sped up. Thus, both response time and recovery time were faster at 250℃, i.e., 27 and 77s, respectively. Additionally, the sensing layer is highly selective to H_2S with almost 300 times higher response upon exposure to interfering gases, including CH_4, CO, methanol, H_2, acetone, ethanol, and He [44] (see Figure 2.7f). The sensor was also reliably stable over 5 months of storage in the air. The increased stability can be attributed to the highly ordered structure of nanorods. Taken together, the porous structures have been shown to significantly enhance the response value at decreased operating temperatures compared to pristine ZnO nanorods. However, the recovery time of porous nanorods was longer than that of the pristine nanorod, which can be attributed to the entrapment of the target gas within its porous structure.

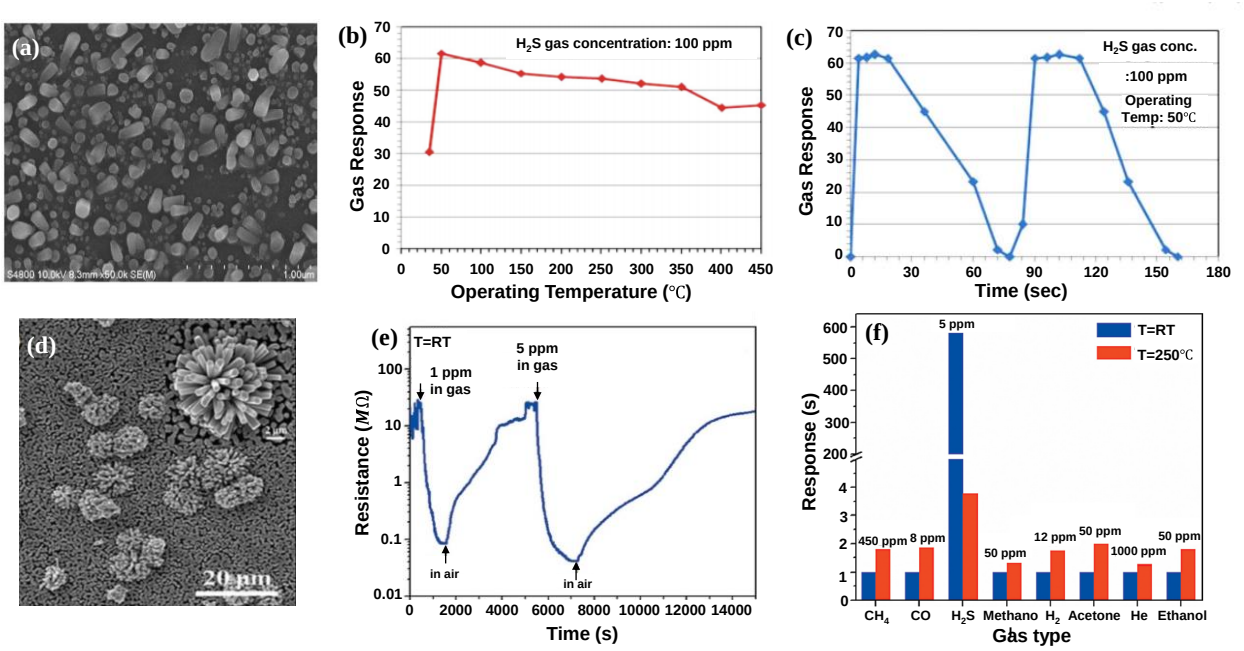

Figure 2.7 (a) SEM image ZnO nanorods. (b) The sensor response is a function of operating temperature. (c) The dynamic behavior of the sensor upon exposure to 100ppm H_2S operating at 50℃. Reproduced from ref. [55]. Copyright © 2012 Elsevier B.V. (d) Top view SEM and (e) Response (I_g/I_a) as a function of H_2S concentration at room temperature upon exposure to 1 and 5ppm H_2S. (f) Sensor selectivity upon exposure to interfering gases. Reproduced from ref. [44]. Copyright © 2014 Elsevier B.V.

In addition to the aforementioned structures, there are a few novel geometries reported in recent studies. These engineered nanostructures are aimed to obtain the desired nanostructure geometry in terms of large surface area (for high response magnitude) and fast response/recovery process. As an example, Zhang et al. [58] reported a dendritic ZnO nanostructure for H_2S room temperature gas sensing. The sensor was fabricated using a horizontal tube furnace. The structure included the main trunk with branches grown at a preferred growth orientation. These parallel branches ranged from 60 to 800nm in diameter and were oriented at an angle of 60° (with respect to the trunk). The crystal structure of the sensing layer was half-octahedral with pyramidal faces. The faces were either (0001) or (000-1), which were terminated by Zn and O, respectively. Because the Zn-terminated face is chemically more active, the possible preferred orientation

growth of the branches was (0001). As the growth process continued, the branches were thickened conjugated with the formation of the interconnected network as the final structure. The all-direction-grown structure provided a large surface area, making it suitable for gas sensing applications. Thus, at a low operating temperature of 30℃ and upon exposure to 10, 50, 100, and 150ppm of H_2S, the response values of 3.3, 11.5, 17.3, and 26.4 ($^{R_a}/_{R_g}$) were obtained. As another positive effect of the increased surface area, the response was fast both in terms of response time and recovery time, i.e., 15-the 20s and 30-50s response time and recovery time, respectively [58]. The response of the innovative dendritic structure is slightly higher compared to that obtained for the pristine nanorod sample, i.e., 3.3 and ~2.8 for dendritic ZnO and ZnO nanorods, respectively. Although the nanorod structure was smaller than the dendritic structure in terms of dimension, the ordered structure of dendritic ZnO provided a larger surface area, overshadowing the effect of smaller dimensions.

Wang et al. [54] are among the first groups to investigate the performance of 2D ZnO nanosheets for low-temperature H_2S gas sensing. The nanosheet fabrication involved the preparation of ZnO powder synthesized by dissolving zinc nitrate salt in NaOH, followed by stirring, washing, and drying. Then, the prepared powder was mixed with terpineol to obtain a paste-like material. The paste was then coated on an alumina substrate using screen printing. The fabricated nanosheets were 30nm thick on average, with almost even thickness throughout the sensing layer. These nanosheets were prone to aggregation and, as a result, formed spheres in a size range of 1-5μm [54]. The highest response obtained for the synthesized nanosheets was at 70℃ with a magnitude of 23 ($^{R_a}/_{R_g}$). The sensor was still sensitive at 60℃ with an acceptable response of 17. Despite these promising properties combined with a linear response and acceptable stability and selectivity, the sensor demonstrated a relatively slow response and recovery times of 252s and 3697s at 70℃, respectively [54]. Although the expected surface area

of a 2D material (nanosheets) is larger than a 3D material (nanorod), the large dimension of the aggregated nanosheets resulted in reduced surface area and thus poor sensing properties.

Overall, compared to thin films, the larger surface area of the nanorods enhanced the response value by about 3.5 times upon exposure to 100ppm H_2S. Moreover, due to the existence of more active sites, both response and recovery processes were faster. Therefore, increasing the surface area of ZnO via physical modification can significantly improve its gas sensing properties, namely, response value, response time, recovery time, and selectivity. A further increase in the surface area can be achieved through the corporation of porous structures (e.g., porous nanorods). However, the porous structure might slow down the kinetics of the recovery reaction due to the entrapment of the target gas in pores. Moreover, the innovative nanostructure can be designed to feature a larger surface area as the surface area plays an important role in the extent of the enhancement.

2.3.2 CuO

CuO is a *p*-type semiconductor material with a narrow band gap of 1.4eV. It has several advantageous properties, such as high thermal stability, high catalyst activity, and non-toxicity. It can be synthesized with different structural and morphological characteristics to meet the needs of the desired application. Therefore, it has a wide range of applications, including optical sensors [59], solar cells [60], electrochemical sensors [61], and gas sensors [62]. This material has been used to detect a variety of gases, from volatile organic compounds (VOCs) [63] to hazardous gases [64]. Despite good gas sensing properties, including high sensitivity, CuO-based sensing layers have a high operating temperature. The high working temperature results in high power consumption and low stability. It was shown that a lower operating temperature can be obtained by manipulating the physical and chemical structure of CuO (summarized in Table 2.2) [65]. However, there is a tradeoff between the low operating temperature and sensor performance.

The main drawback of low-temperature CuO-based sensing layers is the long and even irreversible recovery time. As CuO is exposed to H_2S, superficial CuS is formed. CuS oxidization happens at temperatures as high as 220℃. Although CuS is slowly oxidized in the air, the response is almost irreversible. One solution to fully recover the sensor is to apply an electric pulse to raise the temperature to the desired value and recover the sensor [66]. As an example, Wu et al. [66] reported a CuO-based sensor with a microflower and surface micro spindles structures. The hydrothermally fabricated nanoflowers ranged from 2 to 2.5μm in diameter with 800nm long spindles on the surface. The response and the operating temperature (during for exposure to 1ppm H_2S) were found to be inversely related to each other, with the optimum operating temperature of 25℃. As temperature decreased, the surface desorption rates increased, resulting in a weaker reaction efficiency on the surface. At the optimum temperature, the response was 9.92 (R_g/R_a) with a response time of 130s. However, the main problem was the slow recovery time. After passing 1650s, the sensor only recovered to 20% of its base value. To fully recover the sensor, a 10-second pulse for 130s was applied to raise the temperature to 300℃. Despite the fact that an electric pulse was needed for recovery, the sensor showed acceptable short-term stability toward 1ppm H_2S for four dynamic cycles, with each cycle recovering at 300℃. Although the systems did not exhibit a significant selectivity, the sensor was able to detect the target gas at ppb-level concentrations, e.g., response value of 1.42 toward 50ppb target gas [66].

To further enhance the sensing properties, including the limit of detection, the CuO nanostructure can be tuned to achieve optimized porosity. Interestingly, the porous structure can also change the character of the CuO-based sensing layer from *p*-type to *n*-type. In a recent study, Li et al. [20] fabricated a porous CuO nanosheet for room temperature H_2S gas sensing using a hydrothermal method. The fabricated nanosheets were about 0.5μm in width and 1.5μm in length, and the pore sizes ranged from 5 to 17nm in diameter (Figure 2.8a). According to the

UV-Vis investigations, the structure band gap was 3.08eV, which was remarkably greater than the CuO bulk sample (i.e., around 1.85ev [67]), having a direct influence on the surface adsorption, and thus, gas sensing [20]. The sensor response as a function of analyte concentration at room temperature shows the magnitudes of 1.25 and 5.01 upon 10 and 200ppb H_2S, respectively, presenting the ppb-level detection of the sensing layer (see Figure 2.8b). The formation of CuS at the surface upon exposure to H_2S decreased the resistance by increasing the connectivity between CuO nanosheet neighbors. Moreover, the porous structure facilitated the adsorption/desorption process, and hence, CuS transformation, resulting in rapid response and recovery times [20], as is illustrated in Figure 2.8c. Response/recovery times were measured as 336/543s upon exposure to 200ppb gas, which is among the fastest data reported in the literature for such a sensor [20]. The fast recovery can also be attributed to the porous structure that facilitated molecular diffusion/desorption. Owing to this property, the sensor also functioned well in terms of reproducibility. The obtained response was stable through five dynamic cycles toward 200ppb H_2S with long-term stability over a month (with only less than a 5% response drift). As shown in Figure 2.8d*,* the sensor was selective toward H_2S with a 5 times higher response to H_2S compared to other gases [20].

As it can be seen in Figure 2.8*,* the sensing mechanism for this porous structure is not among the commonly reported ($^{R_a}/_{R_g}$) value for a *p*-type semi-conductor, i.e., the resistance decreased upon exposure to H_2S. In *p*-type semiconductors, the conductivity decreases upon exposure to reducing gases, while the opposite was measured in this study. As mentioned, *p*-type CuO is converted to metallic CuS upon exposure to H_2S (see Equation (2.3). The formed CuS covers the CuO surface and continues to relocate CuO with Cu_xS in sublayers. Thus, due to the metallic-like nature of CuS, conductivity increases and resistance decreases upon exposure to H_2S [20].

$$CuO_{(s)} + H_2S_{(g)} \rightarrow CuS_{(s)} + H_2O_{(g)} \quad (2.3)$$

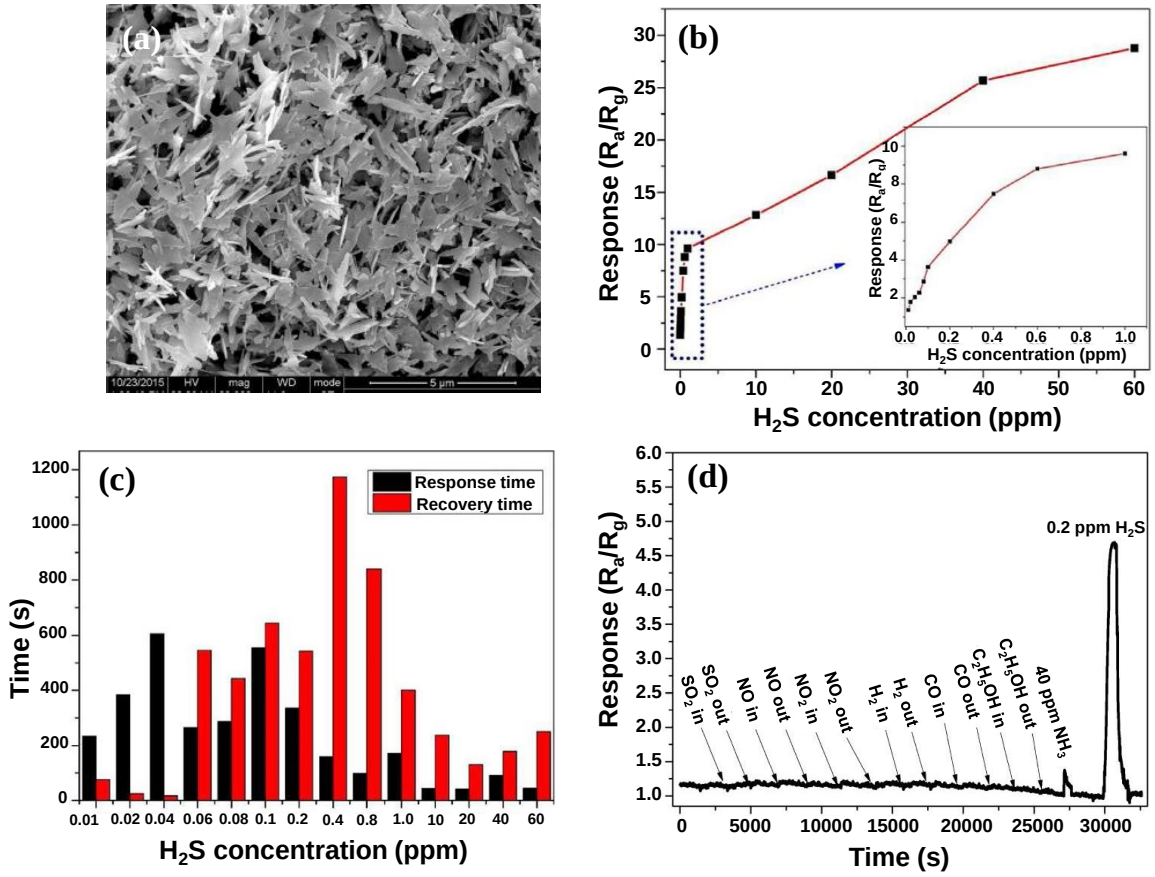

Figure 2.8 (a) SEM image of the structure showing the porous nanosheet structure. (b) Sensor response ($^{R_a}/_{R_g}$) as a function of the analyte concentration, showing ppb-level of detection of the sensing layer. (c) Response and recovery time magnitudes for different gas concentrations. (d) Sensor response upon exposure to different interfering gases with an acceptable selectivity toward H_2S. Reproduced from ref. *[20]* .Copyright © 2016 American Chemical Society.

In another study, Li et al. [68] reported a flower-like porous nanosheet for H_2S gas sensing using a porous nanostructure. The sensing layer was fabricated using a hydrothermal method on a tubular alumina substrate. Based on the SEM images, 60nm thick nanosheets were aggregated in flower-like structures with pores ranging from 20 to160nm in diameter (Figure 2.9a). The mechanism of formation of 2D plate-like structures can be explained as follows: $NH_3.H_2O$ was

added drop by drop to the precursor solution containing Cu ions. The resulted chemical reaction can be described as:

$$Cu^{2+} + 4NH_3 \rightarrow [(CuNH_3)_4]^{2+} \quad (2.4)$$

The product of the above reaction, which is favorable in forming a 2D structure, reacted with hydroxide ion in the precursor solution, forming $Cu(OH)_2$ layer. $[(\mathrm{CuNH_3})_4]^{2+}$ transports Cu^{2+} ions to where OH^- ligands were attached. This assembly released NH_3 and as time elapsed, formed long chains. These chains further grew laterally, forming the final nanosheet structure [68, 69]. The sensor response as a function of gas concentration ranging from 100ppb to 20ppm at room temperature is shown in Figure 2.9b. The results show that the sensor was sensitive down to ppb levels. The response magnitude upon exposure to 1ppm was reported 2.01 with 240 and 1341s as response and recovery times, respectively (see Figure 2.9c), which are among the slowest reported in the literature. The obtained response was stable over 5 dynamic cycles and reproducible over 30 days with less than 3% drift [68].

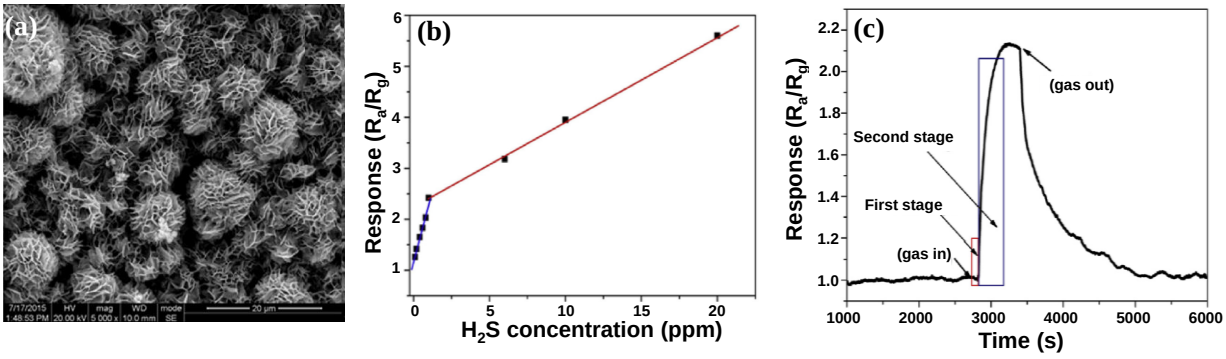

Figure 2.9 SEM image of porous CuO nanosheets aggregated in a flower-like structure. (b) Sensor response as a function of the H_2S concentration showing a 0.1ppm limit of detection. (c) Dynamic response upon exposure to 1ppm H_2S at room temperature showing a slow recovery process. Reproduced from ref. *[68]*.

Pore size is one of the most important parameters in the determination of the nanostructured gas sensing properties. While the porous structure can facilitate the

adsorption/desorption process, large pore sizes might trap H_2S gas molecules and interfere with the recovery process. An excellent example is a comparison between porous CuO nanosheets and flower-like porous CuO nanosheets where pore sizes were reported to be 5-17 and 20-160nm, respectively. Smaller pore sizes decreased the recovery time from 1341s down to 543s.

CuO nanostructures with a large surface area such as spindle-like and nanosheet structures can be efficient candidates for the room-temperature sensing of H_2S at ppb levels. However, the long recovery process still remains their major problem. As discussed, CuO-based sensing layers suffer a long recovery process due to the slow oxidation of CuS in the air. Hence, the CuO-based sensors normally do not recover at room temperature. The introduction of a porous nanostructure can facilitate the desorption process, and therefore improving the sensor recovery at room temperature, as well as lowering the limit of detection down to ppb levels. However, the optimization of the pore size still remains a key challenge. In conclusion, CuO nanostructures with a large surface area can be efficient candidates for sensing ppb levels of H_2S. However, the long recovery process still remains their major problem.

2.3.3 In_2O_3

In_2O_3 is an important *n*-type Ⅲ-Ⅴ semiconductor with a wide bandgap of 3.6 eV. In_2O_3 shows excellent gas sensing properties resulting from great catalytic performance. In_2O_3 has been fabricated in different geometries (e.g., porous thin film [70], nanorod [71], nanowire [72], nanofiber [73], etc.) to detect H_2 [74], NO_2 [75], CO [76], and ethanol [77]). It has also been widely reported for H_2S gas sensing (summarized in Table 2.2). Unlike other metal oxide-based gas sensors, most of the In_2O_3 based sensing layers have low operating temperatures. As an example, Bari et al. [78] fabricated In_2O_3 thin film for low-temperature H_2S sensing. The films were fabricated using a spray pyrolysis method at various thicknesses (e.g., 10, 20, 30, 40, and 50nm) by manipulating the deposition time. The final structure consisted of roughly spherical particles with an average size of 36nm along with large clusters (due to the particles aggregation). The

sample with 30nm thickness showed the highest sensitivity of 79% at the optimum operating temperature of 50℃ upon exposure to 500ppm target gas. The structure was selective to H_2S in a mixture of seven interfering gases. Moreover, the response was reported to be stable for only three cycles with a fast response time and recovery time of 4 and 8s, respectively. These magnitudes are among the fastest ones reported in low-temperature sensing applications. The high and fast response can be attributed to the porous-like structure of the thin film, providing large surface area [78].

To further enhance the gas sensing properties of the thin film structure, including the optimum working temperature and response value, surface area should be further increased. An ordered nanoparticle structure rather than randomly aggregated nanoparticles can help improve the specific area. An example is a recent study conducted by Wang et al. [79], in which the reported sensing layer was a micro-nano porous In_2O_3 thin film for low-temperature H_2S gas sensing. First, the pre-structured colloidal template was fabricated using a self-assembly method on a glass substrate. Then, the template was dip-coated in an indium nitrate precursor solution. The dip-coated template was then placed into a pre-fabricated electrode alumina tube, followed by calcination at 300℃ to form the final ordered thin-film structure [79]. According to TEM and FESEM images, In_2O_3 nanoparticles were fabricated with an average size of 20nm, aggregated in the template form (see Figure 2.10a). In order to study the gas sensing properties of the fabricated sensors, first, the response was measured as a function of the analyte concentration at room temperature. As it is shown in Figure 2.10b, the sensor was almost saturated after exposure to 1ppm, and for higher concentrations, the response was independent of the analyte concentration. The sensor dynamic response was also studied upon exposure to 50ppm H_2S. Although the sensor response was rather fast, i.e., 140s, it did not fully recover at room temperature (Figure 2.10c). Even after 4500s, the sensor still did not get back to the baseline value. It was finally fully recovered after being heated up to 300℃ [79].

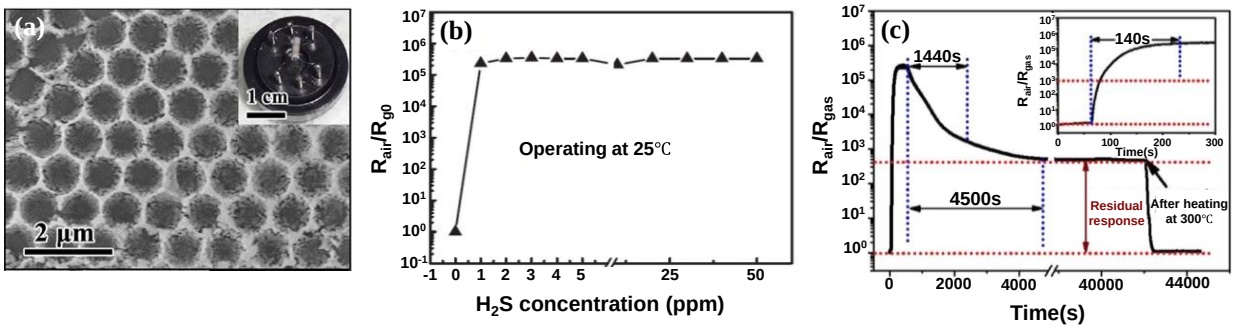

Figure 2.10 (a) FESEM image of an In_2O_3 porous thin film with the template-based structure. (b) Sensor response ($^{R_a}/_{R_g}$) as a function of the H_2S concentration operated at room temperature. (c) The dynamic response upon exposure to 50ppm H_2S, showing the sensor irreversibility after 4500s. Full recovery was achieved after it was heated to 300℃. Reproduced from ref. [79]. Copyright © 2016 Elsevier B.V.

There are different parameters that determine the final structure of the metal oxide, such as the agents and their proportional ratios in the precursor solution, the calcination time, and temperature. As an example, Xu et al. [80] studied the differences in gas sensing properties of porous nanotubes and porous nanowires array. Both structures were fabricated with almost the same procedure, i.e., dissolving an appropriate amount of indium nitrate in DMF followed by the addition of a certain amount of polyvinylpyrrolidone (PVP) to make the desired In/PVP ratio. Afterward, the fabrication process continued by vigorous spinning and then loading the In/PVP suspension in a plastic syringe for electrospinning. The resulted fibers were dried and annealed, forming the final structure. Before the heat treatment, the structure consisted of fibers with diameters of 250, 300, and 350nm, depending on the In/PVP ratio. However, after the heat treatment and as the In/PVP ratio increased, the continuous fiber structure shrunk to nanotubes and nanowires with diameters of 80 and 120nm, respectively. The final geometry, i.e., nanotubes or nanowires, depended on the In/PVP ratio [80]. For instance, as it can be seen in Figure 2.11a, for the ratio of 0.36, nanotubes were obtained with a wall thickness of 15nm. Another main parameter in determining the final structure was the annealing temperature. As the annealing

temperature increased, the reaction rate at the inner sites was higher than the reaction rate at the outer sites. As a result, the inner ones expanded and formed nanotubes, while the outer particles shrunk.

The sensor responses as a function of the operating temperature for different In_2O_3 nanostructures are shown in Figure 2.11b. There is an inverse relationship between the response magnitude and the operating temperature in both nanotubes and nanowires, making the room temperature the optimum operating temperature. Both nanotubes and nanowires showed a high response to 20ppm H_2S, reported as 166.6 and 141.1 (R_a/R_g), respectively. The sensing layer was found to be selective to H_2S in the presence of 20ppm interfering gases (see Figure 2.11c) [80]. In addition to long-term stability over 140 days, the response and the recovery reactions were rather fast. The response/recovery times of 289s/636s and 199s/317s were obtained for nanotubes and nanowires, respectively, and the values increased with temperature. The reason for this increase in the recovery/response time with temperature can be attributed to the fact that the reaction barrier height increases with temperature, requiring more energy to overcome the barriers. As a result, the response and recovery kinetics were slower at higher temperatures [80].

In a similar study, Duan et al. [81] reported a toruloid In_2O_3 nanotube for low-temperature H_2S gas sensing. The electrospinning method was used to fabricate the nanotubes. A novel method was suggested by the authors regarding the preparation of the precursor solution, i.e., the addition of mineral oil. After dissolving indium nitrate in 2g DMF and 4g ethanol, 0.002 and 0.004g mineral oil were added to the solution, named as TNTs-1 and TNTs-2, respectively. For the sake of a better comparison, nanofibers were also fabricated using the same method but without mineral oil. The response value was investigated upon exposure to 50ppm H_2S as a function of the operating temperature. The highest response for TNTs-2 is obtained at room temperature with a magnitude as high as 320.14. The value is about 1.5 times greater than those obtained for nanofibers without mineral oil in the precursor solution at the same operating

temperature. The reason can be attributed to the larger surface area provided by nanotubes. Also, the response and recovery times for the optimum sample were reported 45 and 127s, respectively [81].

In an interesting study, Kaur et al. [82] designed an engineered In_2O_3 nanowhisker structure to further enhance the surface area for low-temperature gas sensing. As shown in Figure 2.11d, nanowhiskers were fabricated with a diameter of 100-300μm and a length of few millimeters using a carbothermal method. The fabricated structure was able to sense H_2S down to ppb levels (Figure 2.11e). Response and recovery times were observed to change with the concentration of the target gas. While the response time decreases as the concentration increased, the recovery time became longer. The sensor response toward 10ppm gas was about 30, which was significantly improved compared to the pristine thin film samples. This improvement was attributed to the existing defects in the whisker structure, which resulted in a larger surface area [82].

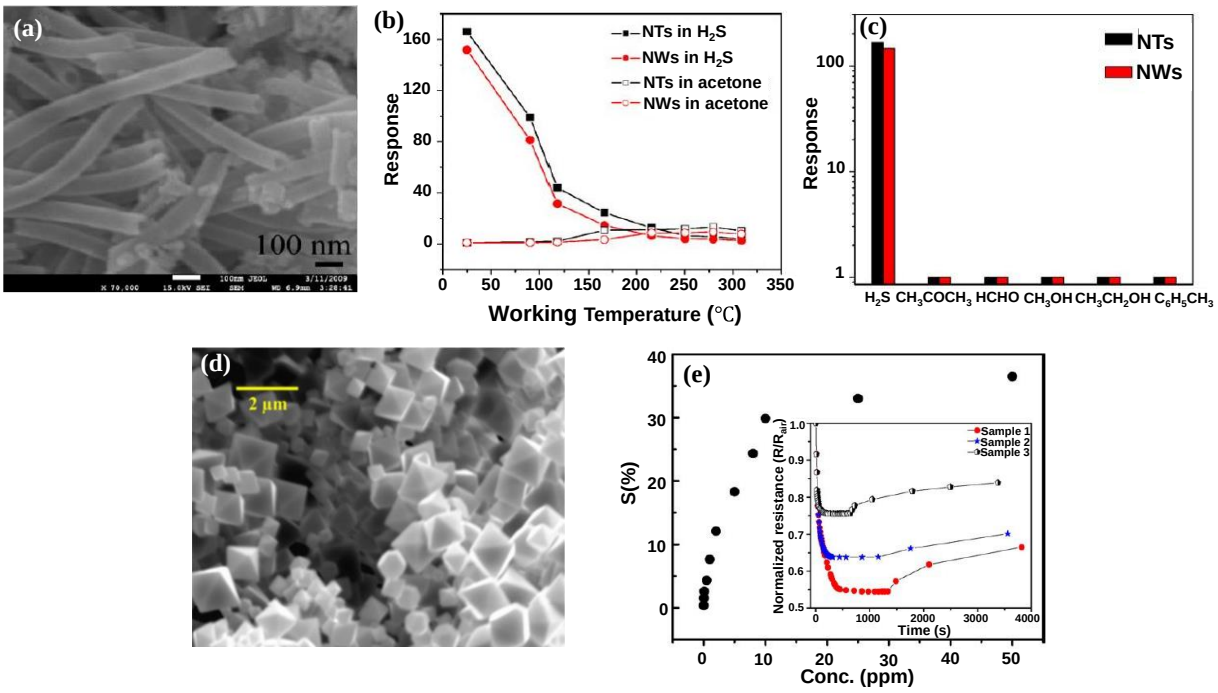

Figure 2.11 (a) FESEM image of In_2O_3 nanotubes annealed at 600℃ with 0.36 In/PVP ratio. (b) The nanotube and nanowire response to 20ppm H_2S versus acetone at room temperature. (c) Sensor selectivity upon exposure to 20ppm H_2S and 20ppm of an interfering gas. Reproduced from ref. [80]. Copyright © 2017 IOP Publishing Ltd. (d) SEM image of In_2O_3 nanowhiskers. (e) The sensor response is a function of the analyte concentration at room temperature. Reproduced from ref. [82]. Copyright © 2008 Elsevier B.V.

Various geometries provide different surface areas, and the surface area plays a key role in the determination of sensing properties in sensing layers with the same materials. Thus, geometry optimization is considered a promising approach to enhance gas sensing properties. Taken together, a porous thin film structure cannot show the desired gas sensing properties at low temperatures, in terms of the response value, even at thicknesses lower than 50nm [78]. However, the conversion of the porous thin film structure into a porous surface, comprising of micro-nano structures, can increase the surface area for a higher response magnitude [79]. The significant impact of the surface area can also be seen in the differences in sensing properties of

In_2O_3 nanotubes [80] and compared to In_2O_3 toruloid nanotubes [81]. Toruloid nanotubes were 8 times smaller in diameter than simple nanotubes; thus, the higher response conjugated with the faster response and recovery times were obtained. However, more studies are required to investigate the gas sensing performance of In_2O_3 in other so-called nanostructures such as nanorods and nanosheets. Overall, pristine In_2O_3-based sensing layers show high sensitivity with an acceptable response/recovery time only if the provided surface area is sufficiently large.

2.3.4 WO_3

WO_3 is an *n*-type semiconductor with a wide indirect bandgap of 2.6-3eV. Unique physical and chemical properties such as chemical stability, superior optical contrast, and mechanical strength have made it a promising candidate for various applications, including photocatalyst [83], electrochromic [84], and photoelectrodes [85]. Although this material has not been widely studied for gas sensing applications, it is deemed as an excellent candidate for hazardous gas detection, such as NO [86], NO_2 [87], NH_3 [88], CO [3], and H_2S [89].

However, most of the aforementioned cases have high operating temperatures. A couple of examples of pure WO_3 based H_2S gas sensors operating at high temperatures are shown in Figure 2.12. Poongodi et al. [90] developed a WO_3-based nanostructured thin film for H_2S sensing. As shown in Figure 2.12a, WO_3 nanostructures were fabricated on a WO_3 seed layer using an electrodeposition method. The obtained nanoflakes were in the range of 10-20nm in thickness and 1μm in height. The highest reported response in the presence of a 10ppm analyte concentration was found to be 85% at 300℃, which is a small magnitude at the mentioned high operating temperature (Figure 2.12b) [90].

In a recent study, Kaur et al. [91] reported a WO_3 nanowire-based H_2S gas sensor. Nanowires were fabricated through a vapor-liquid-solid (VLS) method on an alumina substrate. To optimize the fabrication process, a thin layer of noble metal was sputtered on the substrate, functioning as a catalyst. The nanowires, as shown in Figure 2.12c, were fabricated with an

average diameter and length of 10-30nm and 100nm, respectively. The optimum operating temperature of the sensing layer was reported to be 400℃, showing a high response with a magnitude of 209 upon exposure to 20ppm H_2S (Figure 2.12d) [91].

Li et al. [92] reported a mesoporous WO_3 structure for H_2S gas sensing. The sensor consisted of a uniformly ordered cubic mesostructured with an average pore size of 10.5nm and a wall thickness of 6.6nm (Figure 2.12e). Investigating the response as a function of the working temperature (a wide range from 150 to 350℃) upon exposure to a 50ppm analyte revealed that the maximum response took place at 250℃. A high response magnitude of 270 and fast response and recovery times of 2 and 38s, respectively, were obtained at the optimum operating temperature of 250℃ (Figure 2.12f) [92].

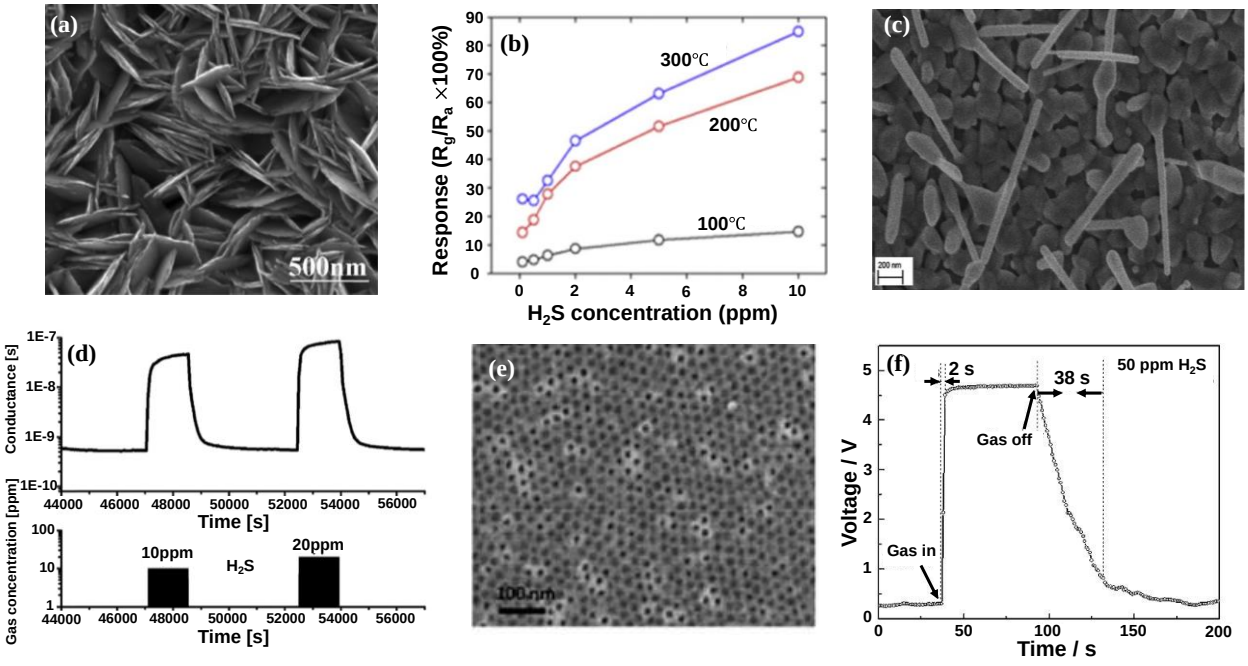

Figure 2.12 (a) SEM image of WO_3 nanoflakes forming a thin film structure, and (b) the sensor response as a function of the analyte concentration in three working temperatures. Reproduced from ref. [90]. Copyright © 2017 Elsevier B.V. (c) SEM image of a WO_3 nanowire structure, and (d) the sensor response and dynamic response upon exposure to 10 and 20ppm H_2S. Reproduced from ref. [91]. Copyright © 2019 American Chemical Society. (e) FESEM image of a mesoporous WO_3 thin film showing a uniformly

ordered structure, and (f) the sensor dynamic response, showing fast response and recovery times. Reproduced from ref. [92]. Copyright © The Royal Society of Chemistry 2020.

Morphology control, which directly impacts the surface area, is one of the best methods to reduce the operating temperature of WO_3 sensing layers (summarized in Table 2.2). San et al. [93] developed a WO_3 nanotubes (NTs) array with a reduced operating temperature for H_2S gas sensing. NTs were fabricated using a thermal evaporation method on a Si substrate, following the vapor-solid (VS) growth mechanism. This process included two steps: nucleation and growth. In the nucleation process, WO_3 was heated to a certain temperature at which the WO_3 vapor was generated. The vapor was then cooled down and condensed on a Si substrate, functioning as the seed layer for NTs to grow on. FESEM images showed that NTs were fabricated with a well-shaped hexagonal cross-section with an average crystal size of 85nm (see Figure 2.13a) [93]. A WO_3 NT-based sensor response as a function of the operating temperature upon exposure to 10ppm H_2S is shown in Figure 2.13b. Although the sensor exhibited the highest response at 150℃ with a magnitude of 7.3, it still showed an acceptable response at the reduced temperature of 50℃. Despite the weak gas selectivity, the sensor showed a reversible response at the optimum operating temperature with a fast recovery time upon exposure to air (see Figure 2.13c) [93].

Overall, pristine WO_3-based sensing layers show high sensitivity toward H_2S; however, their high operating temperature has restricted their applications in low-temperature gas sensing. Their sensing properties can be effectively improved by chemical modifications, elaborated in the next section.

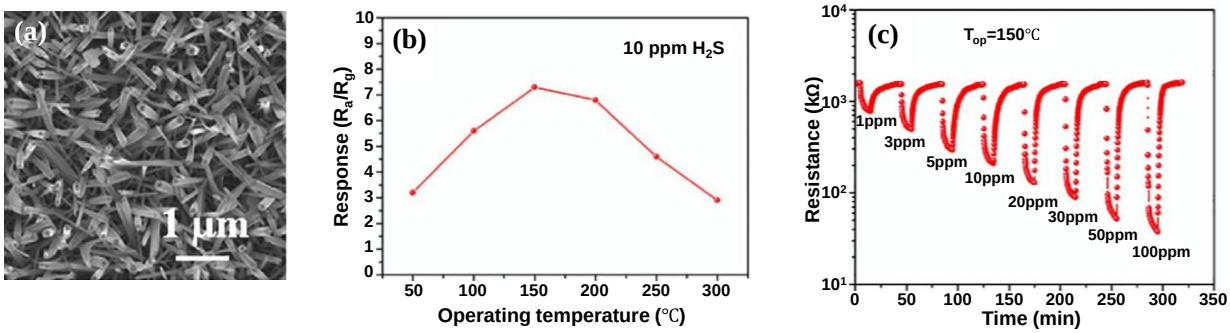

Figure 2.13 (a) FESEM image of a fabricated WO_3 nanotube array showing a well-shaped hexagonal structure. (b) The sensor response is a function of the operating temperature with the optimum operating temperature of 150℃. (c) The sensor dynamic response upon exposure to different H_2S concentrations at the optimum operating temperature. Reproduced from ref. [93]. Copyright © 2020 Elsevier B.V.

Table 2.2 List of Low-temperature H_2S gas sensors.

Material	Response formula	Response	H_2S concentration (ppm)	Working temperature (℃)	Response time (s)	Recovery time (s)	Ref.
ZnO nanosheet	R_a/R_g	23	100	70	252	3697	[54]
ZnO nanosheet	R_a/R_g	17	100	60	-	-	[54]
ZnO nanorod	R_a/R_g	61.7	100	50	4	60	[55]
ZnO nanorod	R_a/R_g	30	100	35	-	-	[55]
Porous flower-like ZnO nanorod	R_a/R_g	581	5	RT	320	3592	[44]
Porous flower-like ZnO nanorod	R_a/R_g	296	1	RT	-	-	[44]
Dendritic ZnO	R_a/R_g	3.3	10	30	10-20	30-50	[58]
Dendritic ZnO	R_a/R_g	26.4	150	30	10-20	30-50	[58]
CuO microflower	R_g/R_a	9.92	1	RT	130	NA	[66]
Porous CuO nanosheet	R_a/R_g	1.25	0.01	RT	233	76	[20]

Porous CuO nanosheet	R_a/R_g	5.01	0.2	RT	336	543	[20]
Flower-like CuO nanosheet	R_g/R_a	2.01	1	RT	240	1341	[68]
In_2O_3 thin film	$\Delta G/G_a$	79%	500	50	4	8	[78]
Porous In_2O_3 thin film	R_a/R_g	340,000	50	RT	140	-	[79]
In_2O_3 nanotube	R_a/R_g	166.6	20	RT	289	636	[80]
In_2O_3 nanowire	R_a/R_g	141.1	20	RT	1999	317	[80]
In_2O_3 toruloid nanotube	R_a/R_g	320.14	50	RT	45	127	[81]
In_2O_3 nanowhisker	$\Delta R/R_a$	30	10	RT	-	-	[82]
In_2O_3 nanowhisker	$\Delta R/R_a$	3.16	0.2	RT	-	-	[82]
WO3 nanotube array	R_a/R_g	3.2	10	50	-	-	[93]

2.4 Section summary

Emerging interest in the development of highly efficient gas sensors has led to comprehensive studies on MOS-based gas sensing. These highly efficient sensing layers should provide a high response value with fast response and recovery kinetics at reduced operating temperatures, preferably, room temperature. In this section, we provided recent advances in ZnO, CuO, In_2O_3, and WO_3 based gas sensors and their advantages and shortcomings for low-temperature H_2S sensing applications.

Based on the data provided in this chapter, ZnO-based sensing layers are among the best candidates for low-temperatures H_2S sensing as they provide acceptable performance in terms of the response value, response time, recovery time, and selectivity. CuO-based sensing layers can provide a rather high response value even down to ppb levels; however, they have slow and

sometimes even irreversible recovery processes. In_2O_3 based sensing layers can also be promising candidates in terms of providing a high response value and fast response and recovery processes; however, the number of studies on their sensing performance is limited, requiring further elaboration and calls for future experiments. WO_3-based sensors also feature a high response value; however, they are operable at relatively high temperatures, which limits their applications for room-temperature gas sensing. The sensing properties of the mentioned metal-oxides have been summarized in Figure 2.14. Based on the provided data, ZnO is the most promising candidate for low-temperature H_2S gas sensing. Therefore, physical modification of ZnO bulk samples to nanostructures seems necessary to improve the room-temperature gas sensor for hazardous gas detection.

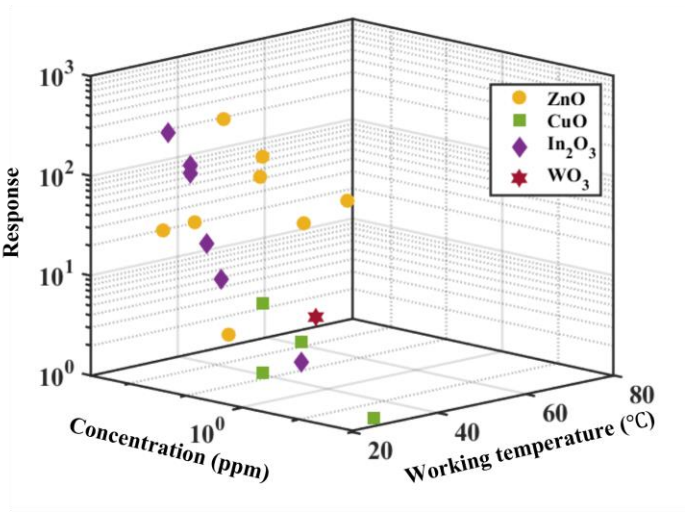

Figure 2.14 3D presentation of MOS-based low-temperature H_2S gas sensors.

Chapter 3: Materials and Methods

This chapter aims to comprehensively explain the synthesis method of flower-like ZnO nanorods, characterization techniques, and gas sensing properties analysis.

3.1 Materials

All chemicals, including zinc nitrate ($Zn(NO_3)_2.6H_2O$), ammonia solution (NH_4OH 28%), ethanol (99.0%), and toluene (99.0%), were purchased from Sigma Aldrich and used without further purification.

3.2 Synthesis of flower-like ZnO nanorods

Two different morphologies of ZnO nanostructures were directly grown on a glass substrate using a modified hydrothermal method. The glass substrates with prefabricated interdigitated electrodes were washed with acetone and sonicated in deionized water/ethanol and dried with N_2. As illustrated in Figure 3.1, 0.5g of $ZnO.6H_2O$ was dissolved in two different ratios of ethanol and deionized water, stirred for 10min at room temperature to form a 40 ml solution. Next, 2ml NH_4OH was added dropwise into the as-prepared solution, and then stirred for 1hr at room temperature. Finally, the glass substrate with prefabricated IDEs was immersed into the precursor solution and sealed in a stainless-steel autoclave for 24hr at 70℃. After the 24hr, the flower-like ZnO nanorods were directly deposited on the glass substrate, and finally, they were annealed for 1hr at 90℃ to form the final sensing layer. Samples with 20/20 ethanol/water and 10/30 ethanol/water were named as S1 and S2, respectively

3.3 Response analysis

A gas sensor is characterized based on six criteria: response value, response time, recovery time, selectivity, stability, and reproducibility. The response value is defined as the ratio of the sensor resistance in steady-state in ambient air over the sensor resistance upon exposure to a target gas (R_a/R_g) and vice versa (R_g/R_a) for a reducing analyte and oxidizing analyte, respectively. The response time and recovery time are defined as the time for the sensor to reach

90% of the total change upon exposure to the target gas and ambient air, respectively. Selectivity is defined as the ability of the sensor to distinguish between different response signals obtained toward different analytes.

To investigate the gas sensing properties of the in-situ deposited flower-like ZnO nanorods (i.e., samples S1 and S2) at room temperature, the gas sensor was placed in a gas testing chamber and exposed to different gas concentrations and connected to an external measurement setup. The changes in the sensing layer resistance upon exposure to different concentrations of different analytes are monitored using Potentistat (VERSASTAT 4) and it is used to investigate its gas sensing properties (i.e., response value, response time, recovery time, selectivity, and long/short-term stability).

The gas chamber is a 40-liter chamber coated with Perylene C to decrease the gas adsorption on the wall. It also includes the following elements: injection valve, fan, heater, compressor (California Air Tools 1P1060S), sensor holder, and temperature and humidity sensor (see Figure 3.1). Different target analytes (e.g., ethanol, isopropanol, 2-pentanol, toluene, N_2O, and H_2S) were employed at different concentrations to investigate the sensing properties of flower-like ZnO nanorods. To obtain the desired concentrations of ethanol, isopropanol, 2-pentanol, and toluene, specific amounts of each analyte (calculated using the chamber volume, analytes density, and molecular weight, ideal gas law, and desired concentration [94]), was directly injected into the gas chamber via the injection inlet using a pipette. The analyte was evaporated with the help of the microheater, and the fan homogenized the airflow in the gas chamber. To obtain the desired concentrations of N_2O and H_2S gas, the gas flow rate was controlled using a mass flow controller and was directly injected into the gas chamber.

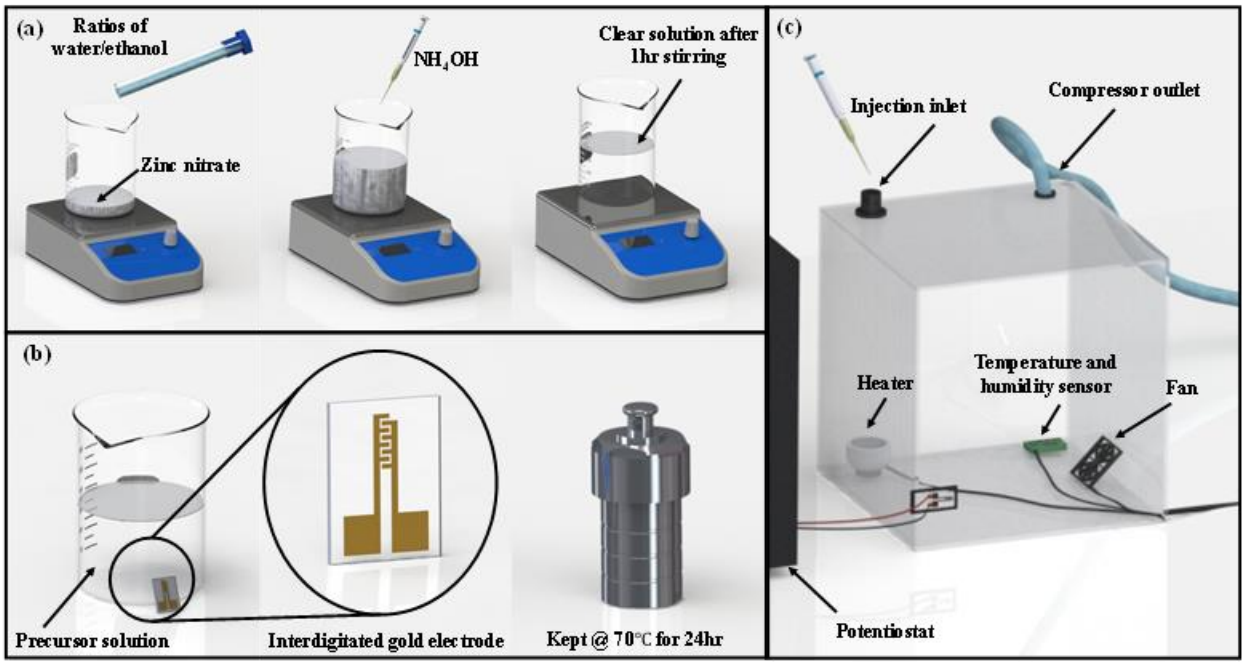

Figure 3.1 Schematics of (a) the steps of the precursor solution preparation, (b) In-situ deposition of the sensing layer, and (c) gas sensing measurement setup.

3.4 Material characterization

3.4.1 Scanning electron microscopy (SEM)

The scanning electron microscope uses a focused electron beam to provide a variety of signals from the surface of the solid sample. SEM images can provide information regarding the sample morphology, topography, composition, and crystalline structure. Generally, SEM characterization works based on the electron and matter interaction. As the electron beam hits the sample, the electrons are either passed through the samples or reflected (see Figure 3.2). Among the reflected electrons, SEM characterization investigates secondary electrons and backscattered electrons, which are reflected as a result of inelastic and elastic interaction between the electron beam and the sample atoms, respectively. Backscattered electrons are reflected from deeper regions of the sample, whereas the secondary electrons are reflected from the surface or near-surface regions. Therefore, backscattered electrons can provide information regarding the

chemical composition contrast and crystalline structure and the secondary electrons can provide great 3D images and sharp edges.

A schematic of an SEM setup is shown in Figure 3.3. The electron beam is produced from an electron gun at the top. The beam follows a vertical path passing through lenses and electromagnetic fields to be focused on the sample. As the beam hits the sample, depending on the electrons' interaction with the sample, different signals are emitted, which are collected in detectors.

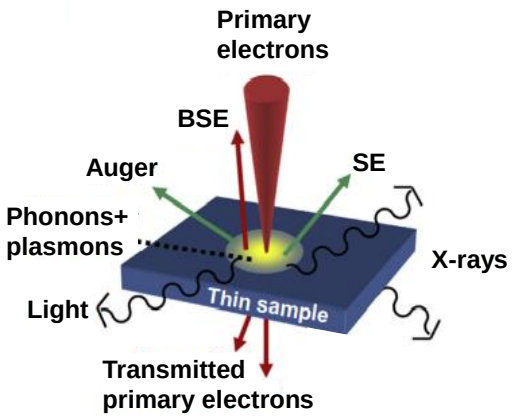

Figure 3.2 Schematic of electron matter interaction. Reproduced from ref. [95]. Copyright © 2016 Elsevier.

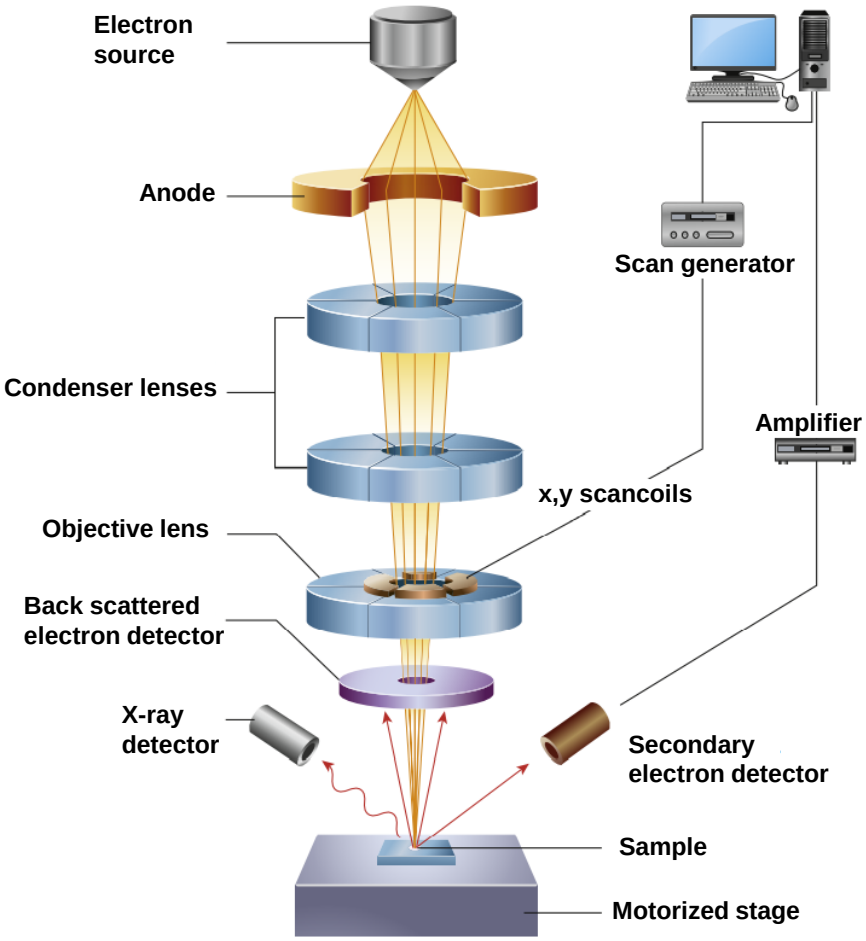

Figure 3.3 Schematic of the scanning electron microscope (SEM). Reproduced from ref. [95]. Copyright © 2016 Elsevier.

3.4.2 X-ray diffraction (XRD)

X-ray diffraction (XRD) is another characterization tool that provides information on the average spacing between layers or rows of atoms, the orientation of a single crystal or a grain, crystalline structure of an unknown material, and the size, shape, and internal stress of small crystalline regions. In this characterization technique, an X-ray beam is emitted through the sample. As the beam passes through the sample, it is diffracted with an angle of θ. The diffracted signals will be detected only if they have constructive interaction, meaning that the waves are whole number integers of the same wavelength. This will result in peaks at specific angles in the

XRD spectra. The diffraction patterns in XRD spectra can be explained based on Bragg's law. Bragg's law is defined as below:

$$n\lambda = 2dsin\theta \quad (3.1)$$

where λ is the wavelength of the X-ray beam, θ is the diffraction angle, d is the atomic layer spacing, and n is an integer. The diffraction angle is specific for different crystalline structures in different materials; therefore, the diffraction pattern can be used to define the crystalline structure and the grain size of the sample.

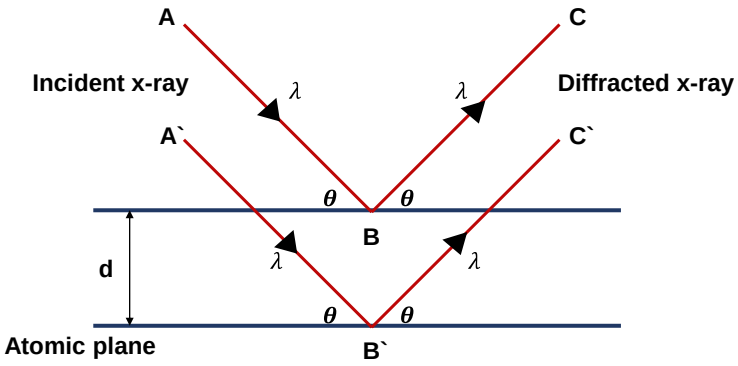

Figure 3.4 Schematic representation of Bragg's law.

3.4.3 X-ray photoelectron spectroscopy (XPS)

X-ray photoelectron spectroscopy (XPS) is a quantitative spectroscopic technique to analyze the surface chemistry of a material. This characterization method emits a beam of X-rays to the sample and simultaneously measures the number and kinetic energy of the electrons escaping from the surface atoms. This characterization technique works based on the photoelectric effect, which is described as follows:

$$E_k = h\upsilon - E_B - \phi \quad (3.2)$$

where E_k is the kinetic energy of the photoelectrons, $h\upsilon$ is the energy of the X-ray beam photons, E_B is the binding energy, and ϕ is the work function. Therefore, binding energy can be calculated by measuring the kinetics of the escaped electrons from the surface. The final XPS spectrum is obtained from measuring the scaped electrons intensity at different kinetics energies.

As shown in Figure 3.5, an XPS setup mainly consists of an X-ray source, extraction lenses, and detector. The XPS instrument is housed in an ultra-high vacuum (UHV) environment to avoid any surface contamination within the sensing chamber and prevent the electrons from scattering off air molecules while reaching the analyzer [96].

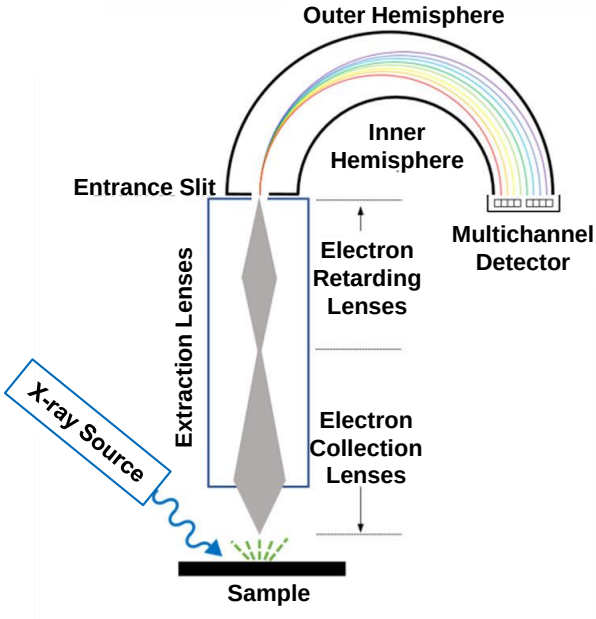

Figure 3.5 Schematic presentation of an XPS setup. Reproduced from ref. [96]. Copyright © 2020 American Vacuum Society.

Chapter 4: Room-temperature Flower-like ZnO Gas Sensor

4.1 Results and discussion

4.1.1 Materials characterization

The crystallinity of the ZnO nanorods was investigated using X-Ray diffraction (XRD) as shown in Fig. 4.1a. The diffraction patterns are well indexed to hexagonal wurtzite ZnO crystalline structure with JCPDS card no. 01-079-0205 [97, 98]. The sharp and strong peak at 36.5° indicates high crystallinity in both samples. However, the peaks are slightly sharper in the S2 sample, implying higher crystallinity in the sample with less ethanol in the precursor solution. Moreover, no other characteristic peaks were observed in the XRD spectra, showing that the crystalline ZnO nanorods were synthesized with high purity and uniformity. According to the Scherrer equation and based on the data extracted from the XRD patterns, the average grain size of samples S1 and S2 were found to be 23 and 19nm, respectively.

The chemical composition of the sample S2 was investigated using X-ray photoelectron spectroscopy (XPS). As it can be seen in Fig. 4.1b, except for a carbon peak (C1s), the full spectra confirmed the high chemical purity of the nanorods consisting of only Zn and O. Fig. 4.1c, shows the Gaussian fitting curves of the O1s spectra of the ZnO nanorods. The peak at 532eV is attributed to the O_2^- ions within the ZnO matrix. Fig. 4.1d shows the magnified XPS spectra of the ZnO nanorods with two peaks at 1022.1 and 1045.3, attributed to $Zn2p_{2/3}$ and $Zn2p_{1/2}$. The observed values are in good agreement with the literature, confirming a ZnO hexagonal wurtzite structure [99].

The hexagonal structure of the ZnO nanorods could also be directly observed from the SEM images. As it can be seen in Fig. 4.2, both nanorod samples feature a uniform hexagonal structure. Moreover, based on the SEM results, the rods in sample S2, are narrower and longer compared to their other counterpart, which can be attributed to the increased kinetics of synthesis reaction due to the lower amount of ethanol in the precursor solution. The EDX results, in Fig.

4.2c and f, only exhibit Zn and O peaks, confirming the high purity ZnO nanorods, which are in good agreement with the previous results.

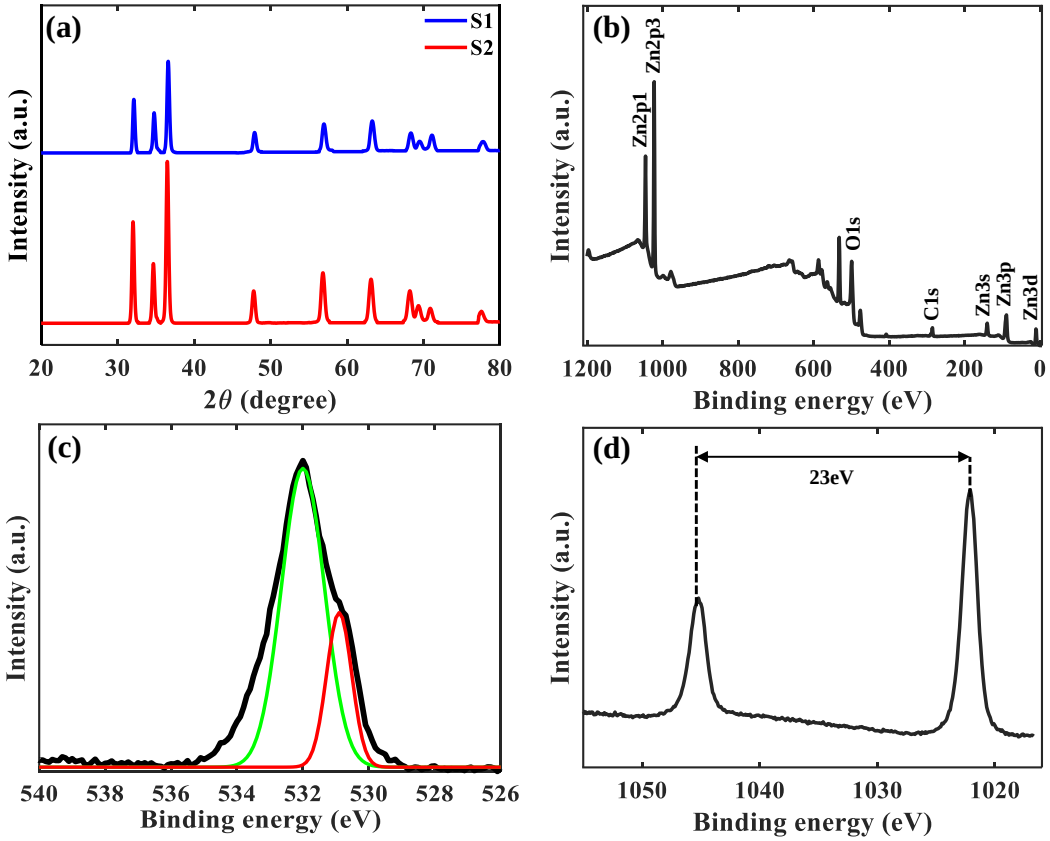

Fig. 4.1 (a) XRD spectra of the samples S1 and S2, XPS spectrum of the ZnO sample S2 (a) full spectrum, (b) O spectrum, and (c) Zn spectrum.

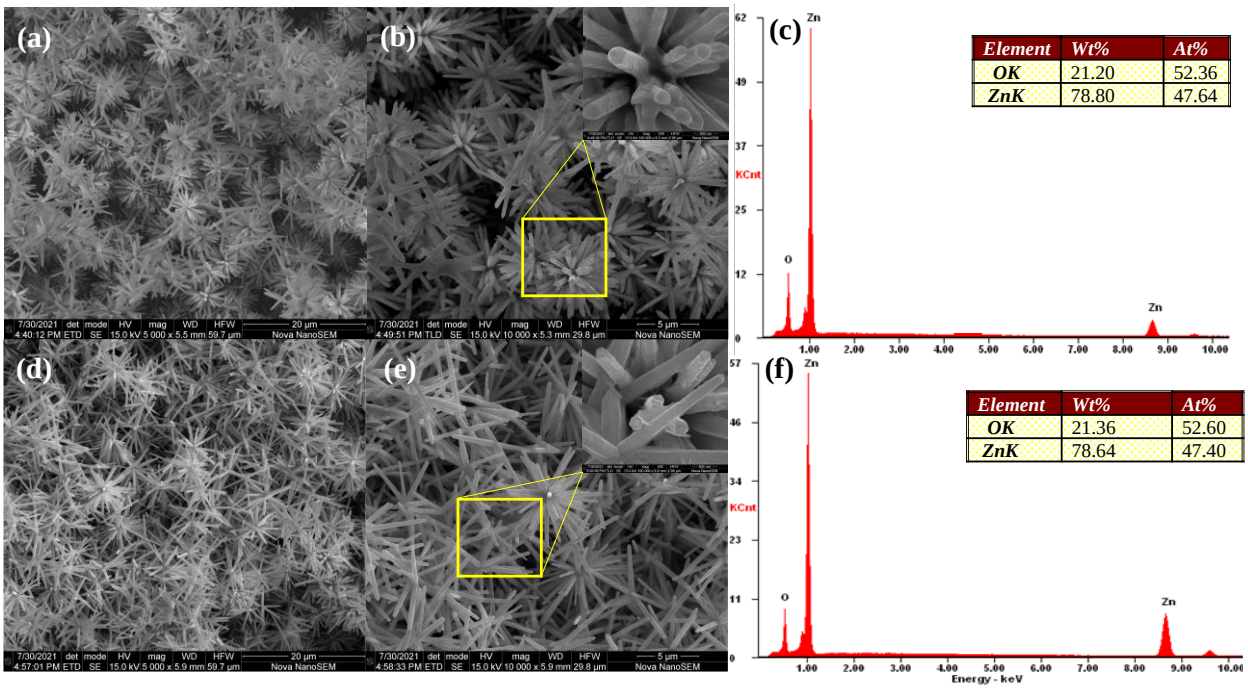

Fig. 4.2. (a, b) and (d, e) SEM images of samples S1and S2 at different magnifications, respectively. (c) and (f) EDX results of samples S1 and S2, respectively.

4.1.2 H_2S gas sensing properties

Samples S1 and S2 were exposed to different concentrations of H_2S gas at room temperature to compare their sensing properties (e.g., response value, response time, and recovery time) and investigate their potential application for room temperature. As presented in Figure 4.3a response as a function of gas concentration shows a linear increasing trend with higher response values obtained from sample S2. Based on the measured values, the sensitivity of samples S1 and S2 were 1.213 and 1.932, respectively. Figure 4.3b, c shows the dynamic response of the samples S1 and S2 upon exposure to 100ppm H_2S. The response value of S1 and S2 was measured 5.4 and 7.4, respectively. The results showed that despite the higher response value of sample S2, the response at recovery kinetics was faster for sample S1, e.g., 206 and 126s for sample S1 and 293 and 186s for sample S2 as response time and recovery time, respectively. The higher response value of sample S2 is attributed to the smaller grain size compared to sample S1. The smaller grain size of the sample S2 results in a higher ratio of

depletion layer width over the conduction bandwidth. Moreover, the lower response and recovery time of a sample of sample S1 is attributed to the lower response value compared to sample S2. The great sensing properties at room temperature can be attributed to a large surface area provided by the lengthy nanorods, as well as a great connection between the rods, which is due to the flower-like structure.

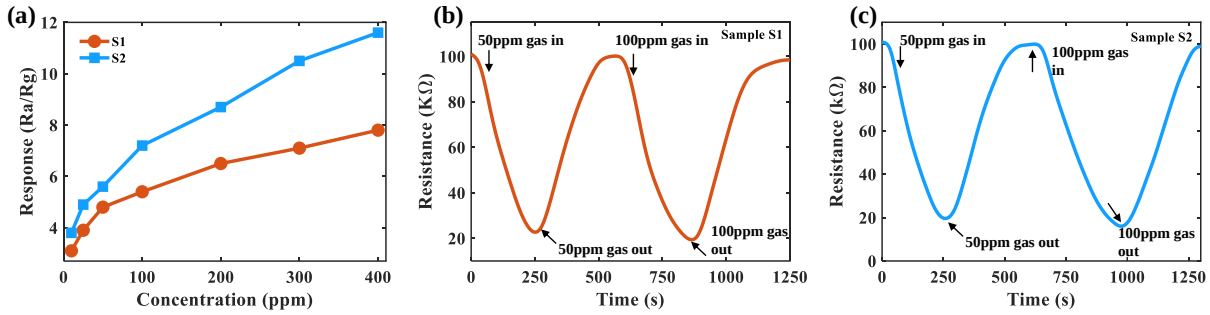

Figure 4.3 (a) The response value as a function of H_2S concentration for samples S1 and S2. The dynamic response of samples (b) S1 and (c) S2 toward 50 and 100ppm H_2S.

Selectivity is another important parameter in the characterization of a gas sensor. As shown in Figure 4.4, both samples S1 and S2 demonstrate an excellent selectivity toward H_2S; however, sample S2 showed a better performance compared with sample S1. The great selectivity performance of both samples can be attributed to a couple of reasons: First, the bond energy of H-HS in H_2S is lower compared with other interfering gases; thus, it can be easily decomposed at room temperature [44, 45]. Second, H_2S is a strong reducing gas, therefore the interaction strength between ZnO and H_2S is higher compared to the other interfering gases. Third, unlike the other interfering gases, the reaction between ZnO and H_2S (which is also called desulfurization reaction) is exothermic. Therefore, the desulfurization reaction can happen simultaneously with the reaction between the adsorbed oxygen species and adsorbed H_2S. Therefore, the spontaneous reaction results in a higher sensitivity toward H_2S [100].

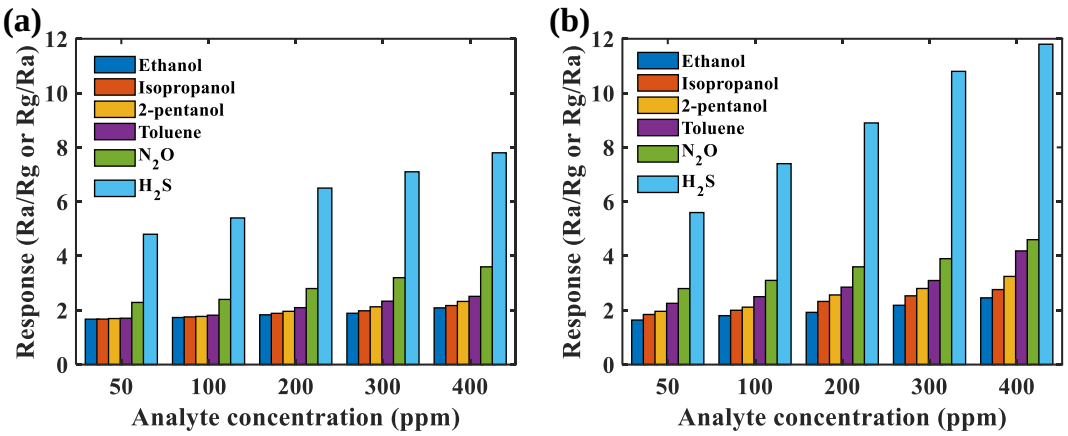

Figure 4.4 The response value of samples (a) S1 and (b) S2 toward different interfering gases at room temperature.

4.1.3 VOC gas sensing properties

In the previous section, we investigated the potential of the flower-like nanorods for H_2S room temperature gas sensing applications. Although the response value toward H_2S was the highest among the interfering gases, the response values toward VOC targets were still acceptable for room temperature gas sensing. Therefore, we have investigated the sensing properties of samples S1 and S2 toward a range of VOCs (i.e., ethanol, isopropanol, 2-pentanol, and toluene) at room temperature. Figure 4.5a, b shows the response value of samples S1 and S2 as a function of analyte concentration toward a range of VOCs. The response as a function of analyte concentration has an increasing trend and the highest response values were obtained from toluene in both samples S1 and S2. The higher response values of sample S2 create a higher bias for the response value range; therefore, the response value toward the target analytes is more distinguishable in sample S2. Figure 4.5c, d shows the dynamic response of samples S1 and S2 upon exposure to the target analytes. As it can be concluded from the graphs, in both samples, the highest response is obtained upon exposure to toluene. The trend in response values for different VOC analytes can be explained by comparing the ionization energy of the

target analytes. It has been found that the energy of the lowest unoccupied energy orbital (LUMO) is inversely related to sensitivity. In other words, the electrons in lower energy orbitals are better captured by the target gas; therefore, the ionization energy of the target gas is inversely related to sensitivity [101, 102]. The ionization energy of ethanol, isopropanol, 2-pentanol, and toluene are 10.62, 10.16, 9.39, and 8.82eV, respectively [101]. The trend in the response values obtained from both samples follows the same trend in ionization energies. The response of sample S1 toward a 100ppm ethanol was stable over four dynamic cycles and over 20 days with negligible response drift (see Figure 4.5e, f). A summary of gas sensing properties of samples S1 and S2 is presented in Table 4.1.

Table 4.1 Summary of gas sensing properties of samples S1 and S2 toward a range of VOCs.

Gas type	S1			S2		
	Response value	Response time (s)	Recovery time (s)	Response value	Response time (s)	Recovery time (s)
Ethanol	1.733	82	75	1.801	145	153
Isopropanol	1.754	72	79	2	148	124
2-pentanol	1.773	65	100	2.115	175	138
Toluene	1.818	190	145	2.5	232	135

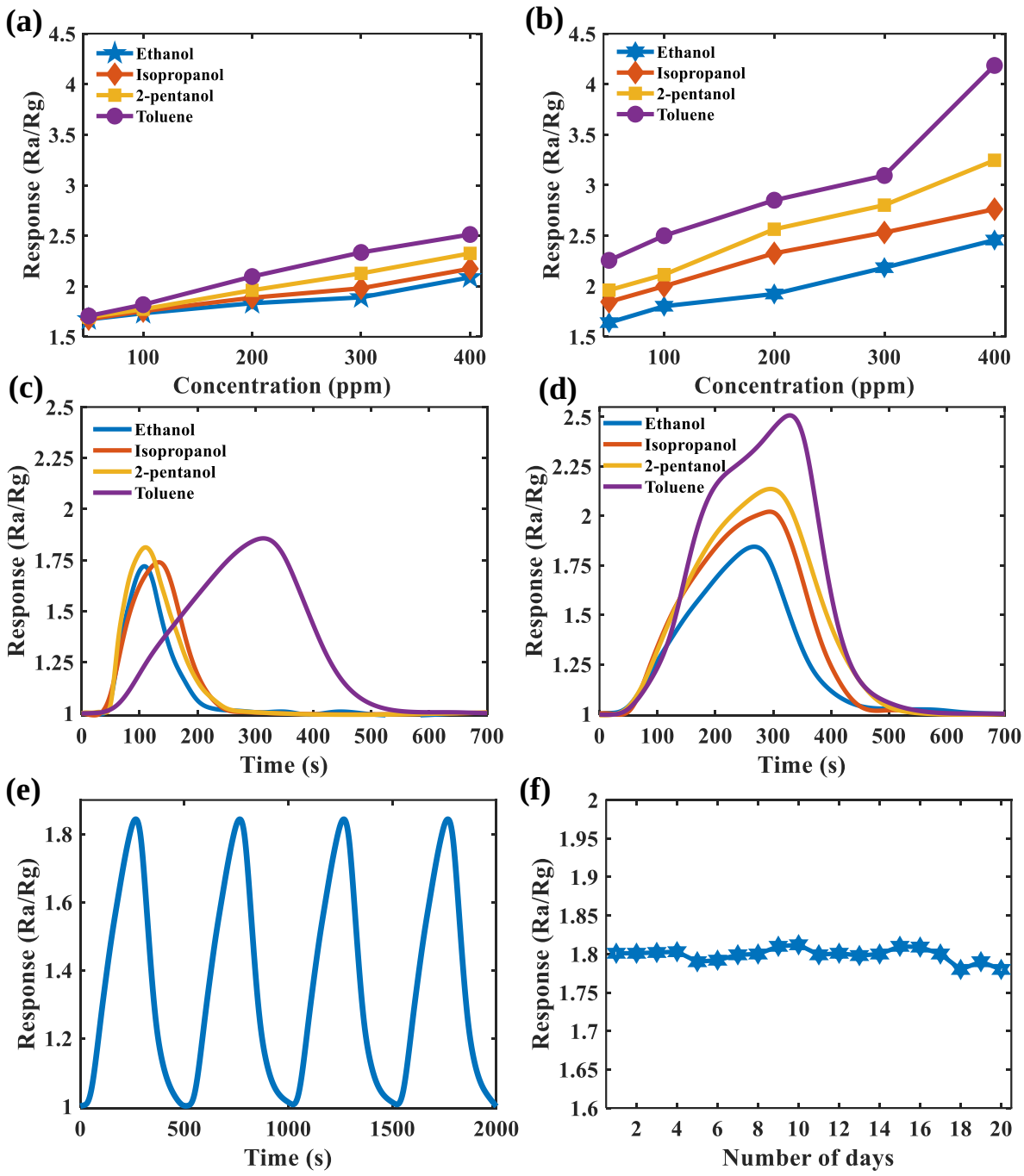

Figure 4.5 The response as a function of analyte concentration for samples (a) S1 and (b) S2 toward a range of VOCs at room temperature. The dynamic response of samples (c) S1 and (d) S2 toward 100ppm target analyte at room temperature. (e) Short-term stability of sample S2 toward 100ppm ethanol over 4 dynamic cycles. (f) Long-term stability of sample S2 toward 100ppm ethanol over 20 days.

4.1.4 Effect of grain size on gas sensing properties

MOS-based sensors work based on the conductivity variation in the sensing layer upon exposure to a target gas. At the steady-state condition, oxygen is adsorbed at the metal-oxide surface in different forms (i.e., O^-, O_2^-, and O^{-2}), depending on the working temperature [103, 104]. The adsorbed oxygen species at the surface of the metal oxide is in the form of O_2^- at room temperature [39]. The oxygen adsorption at the surface of the metal oxide creates an electron depletion layer on the surface of an n-type semi-conductor (a type of semiconductor in which the majority of charge carriers are electrons) [105]. As the sensing layer is exposed to a target gas, the adsorbed oxygen species react with the target gas, changing the width of the depletion layer, and therefore, the sensor conductivity (see Figure 4.6). It should be borne in mind that the magnitude of the change in electrical conductivity is proportional to the gas concentration [52].

One of the most important parameters that affect the gas sensing properties is the width of the depletion layer in the steady-state condition, which is highly impacted by the nanorod dimension. When a metal oxide starts to crystallize, many small sections are formed in different sizes and crystalline orientations. The collection of these regions, which are called grains, forms the final crystalline structure. The average size of the grains determines different mechanical and electrical properties of the metal oxide, including the gas sensing properties. In a crystalline structure, if the average grain size is smaller than the Debye length (λ_D), the conduction band becomes fully depleted. In this case, the metal oxide is highly sensitive, and the sensing properties highly depend on the rod diameter [106]. On the other hand, if the grain size is significantly larger than the Debye length, the conduction band becomes partly depleted [107], and the surface interactions have a less significant effect on the entire layer's conductivity [108]. In other words, in partly depleted sensing layers, the response resistance value is directly affected by the ratio of the width of the depletion layer over the width of the conduction band [107]. This ratio is highly

affected by the grain size. In nanostructures with smaller grain sizes, this ratio tends to be higher in magnitude compared with those with larger grain sizes [107, 109].

In this study, we calculated the average grain size using the XRD data. The average grain size of samples S1 and S2 were 23 and 19nm, respectively, which means these sensing layers belong to the partly depleted conduction band category. Therefore, the response values obtained from sample S2 are expected to be higher compared to sample S1. Figure 4.7 presents a comparison between the response values of samples S1 and S2 toward ethanol, toluene, N_2O, and H_2S at room temperature. Comparing the results obtained from samples S1 and S2, the response value was increased 8%, 27.5%, 29.8%, 39.2% toward ethanol, toluene, N_2O, and H_2S, respectively, in sample S2. The greater response increase toward H_2S can be attributed to the higher response value, which created a higher bias in response values.

Overall, the results indicate the effect of grain size on gas sensing properties, especially response value. In the case of partly depleted nanostructures, the ratio of the width of the depletion layer over the width of the conduction band is one of the key parameters that determines the response value. In nanostructures with smaller grain size, the ratio tends to be higher; therefore, the response values of sample S2 were higher compared with sample S1 toward a specific target analyte. Moreover, along with the average grain size, the target analyte can be an effective parameter in the final gas sensing properties. The response increase was the highest toward H_2S, which implies for the same average grain sizes, the higher response value can result in more distinguishable results comparing nanostructures with different average grain sizes.

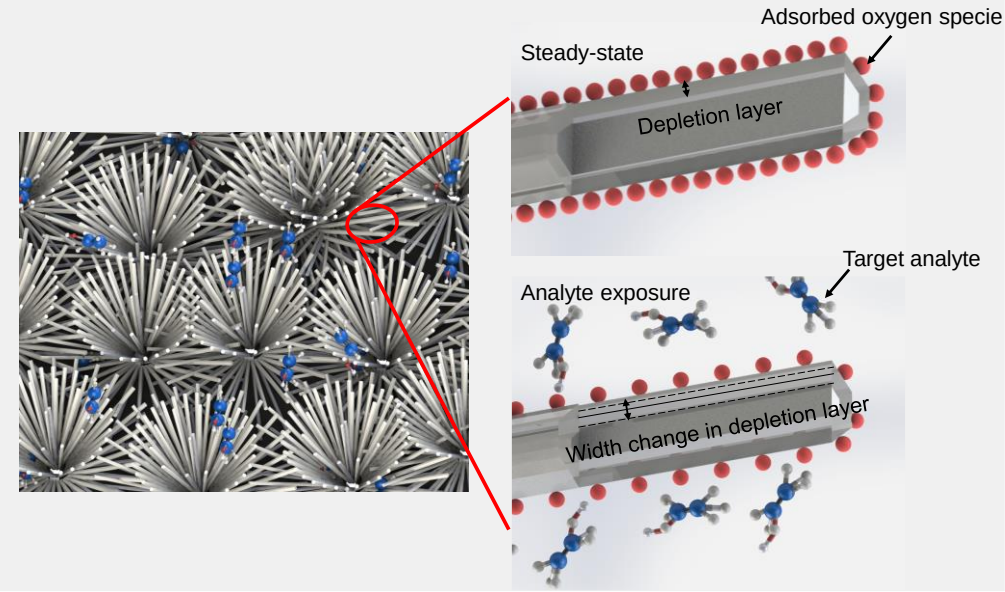

Figure 4.6 Schematic of the gas sensing mechanism of the flower-like ZnO nanorods.

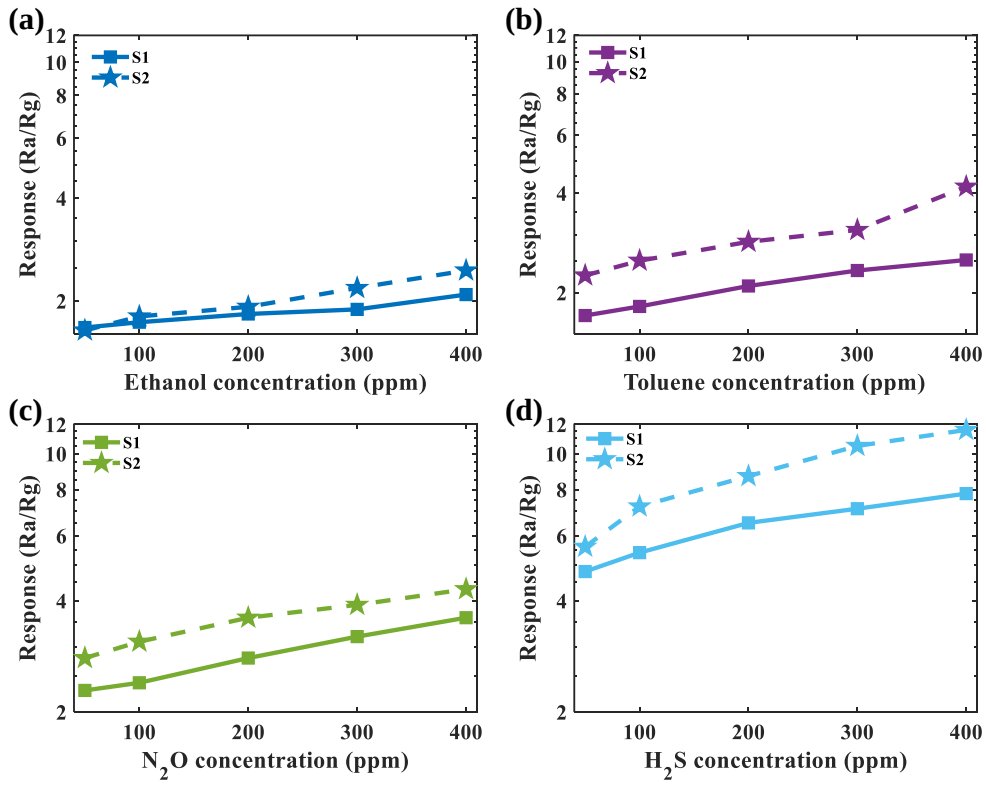

Figure 4.7 The response as a function of analyte concentration for samples S1 and S2 toward (a) ethanol, (b) toluene, (c) N_2O, and (d) H_2S at room temperature.

Chapter 5: Conclusion and future works

5.1 Results summary

We developed flower-like ZnO nanorods using a modified hydrothermal method. The nanorod samples were fabricated in two different grain sizes, i.e., 19 and 23nm. The sample with a smaller grain size provided 7.4 as response value as well as fast response and recovery time of 293 and 186s, respectively, at room temperature. The response was stable in four dynamic cycles and over 20 days with negligible response drift. Moreover, the sensing layer was sensitive to 1ppm of H_2S with a great response value of 3.8, which implied the ppb-level of detection of this sample. Both of the ZnO nanorod samples were capable of selective detection of H_2S among a range of interfering gases. We also investigated the gas sensing performance of both samples toward a range of VOCs, i.e., ethanol, isopropanol, 2-pentanol, and toluene. The highest response value was obtained toward toluene. 2.5 response values and 232 and 135s response time and recovery time, respectively, were obtained toward 100ppm toluene at room temperature. Finally, we investigated the effect of grain size on gas sensing properties, especially response value. It was observed that the sample with a smaller grain size provides higher response values. In this regard, comparing the response values in both samples, an average of 8%, 27.5%, 29.8%, 39.2% response increase was measured toward ethanol, toluene, N_2O, and H_2S, respectively. Overall, the results indicate the potential of the sensing layer in real-time monitoring and detection of hazardous gases, especially H_2S, and provide insights towards future improvements of room temperature gas sensing.

5.2 Future works

- Chemically modify ZnO nanostructures (e.g., incorporating another metal-oxide or a graphene-based material) for enhanced gas sensing properties, especially faster response and recovery kinetics. Incorporation of an p-type semiconductor with ZnO, will create p-n junctions at the surface of the metal oxide, which results in higher response

value. Moreover, the addition of highly conductive nanomaterials such as rGO, can enhance the response and recovery kinetics.

- Enhance the long-term stability of the sensor via further physical and chemical modification.
- The thickness of the sensing layer can be increased using a more active substrate than glass such as alumina or silicon.
- The selectivity of samples S1 and S2 can be investigated toward a range of sulfide-based gases to decrease the cross-sensitivity.
- Samples S1 and S2 are different in surface area as well as their grain size. The surface area of the samples can be investigated using BET analysis.
- Investigate the potential of the existing sensing layer as a self-powered gas sensor.

Bibliography

[1] Z. Wen *et al.*, "Blow-driven triboelectric nanogenerator as an active alcohol breath analyzer," *Nano Energy,* vol. 16, pp. 38-46, 2015.

[2] K.-W. Kao, M.-C. Hsu, Y.-H. Chang, S. Gwo, and J. A. Yeh, "A sub-ppm acetone gas sensor for diabetes detection using 10 nm thick ultrathin InN FETs," *Sensors,* vol. 12, no. 6, pp. 7157-7168, 2012.

[3] M. Hübner, C. Simion, A. Haensch, N. Barsan, and U. Weimar, "CO sensing mechanism with WO3 based gas sensors," *Sensors and Actuators B: Chemical,* vol. 151, no. 1, pp. 103-106, 2010.

[4] D. Zhang, C. Jiang, Y. Yao, D. Wang, and Y. Zhang, "Room-temperature highly sensitive CO gas sensor based on Ag-loaded zinc oxide/molybdenum disulfide ternary nanocomposite and its sensing properties," *Sensors and Actuators B: Chemical,* vol. 253, pp. 1120-1128, 2017.

[5] D. Yang *et al.*, "Gas sensor by direct growth and functionalization of metal oxide/metal sulfide core–shell nanowires on flexible substrates," *ACS applied materials & interfaces,* vol. 11, no. 27, pp. 24298-24307, 2019.

[6] K.-R. Park, H.-B. Cho, J. Lee, Y. Song, W.-B. Kim, and Y.-H. Choa, "Design of highly porous SnO2-CuO nanotubes for enhancing H2S gas sensor performance," *Sensors and Actuators B: Chemical,* vol. 302, p. 127179, 2020.

[7] L. Skrtic, "Hydrogen sulfide, oil and gas, and people's health," *Energy,* pp. 1-77, 2006.

[8] S. Ghaderahmadi, M. Kamkar, N. Tasnim, M. Arjmand, and M. Hoorfar, "A review of low-temperature H 2 S gas sensors: fabrication and mechanism," *New Journal of Chemistry,* 2021.

[9] H. Du, W. Yang, W. Yi, Y. Sun, N. Yu, and J. Wang, "Oxygen-plasma-assisted enhanced acetone-sensing properties of ZnO nanofibers by electrospinning," *ACS applied materials & interfaces,* vol. 12, no. 20, pp. 23084-23093, 2020.

[10] F. Wang, K. Hu, H. Liu, Q. Zhao, K. Wang, and Y. Zhang, "Low temperature and fast response hydrogen gas sensor with Pd coated SnO2 nanofiber rods," *international journal of hydrogen energy,* vol. 45, no. 11, pp. 7234-7242, 2020.

[11] Y. Wang, X.-n. Meng, and J.-l. Cao, "Rapid detection of low concentration CO using Pt-loaded ZnO nanosheets," *Journal of hazardous materials,* vol. 381, p. 120944, 2020.

[12] U. T. Nakate, R. Ahmad, P. Patil, Y. Yu, and Y.-B. Hahn, "Ultra thin NiO nanosheets for high performance hydrogen gas sensor device," *Applied Surface Science,* vol. 506, p. 144971, 2020.

[13] Z. Cai and S. Park, "Synthesis of Pd nanoparticle-decorated SnO2 nanowires and determination of the optimum quantity of Pd nanoparticles for highly sensitive and selective hydrogen gas sensor," *Sensors and Actuators B: Chemical,* vol. 322, p. 128651, 2020.

[14] M. Tonezzer, "Selective gas sensor based on one single SnO2 nanowire," *Sensors and Actuators B: Chemical,* vol. 288, pp. 53-59, 2019.

[15] X. Tong, W. Shen, X. Chen, and J.-P. Corriou, "A fast response and recovery H2S gas sensor based on free-standing TiO2 nanotube array films prepared by one-step anodization method," *Ceramics International,* vol. 43, no. 16, pp. 14200-14209, 2017.

[16] K.-S. Choi and S.-P. Chang, "Effect of structure morphologies on hydrogen gas sensing by ZnO nanotubes," *Materials Letters,* vol. 230, pp. 48-52, 2018.

[17] J. Liu, L. Zhang, J. Fan, B. Zhu, and J. Yu, "Triethylamine gas sensor based on Pt-functionalized hierarchical ZnO microspheres," *Sensors and Actuators B: Chemical,* vol. 331, p. 129425, 2021.

[18] S. Zhao *et al.*, "Complex-surfactant-assisted hydrothermal synthesis of one-dimensional ZnO nanorods for high-performance ethanol gas sensor," *Sensors and Actuators B: Chemical,* vol. 286, pp. 501-511, 2019.

[19] H. Kim, Y. Pak, Y. Jeong, W. Kim, J. Kim, and G. Y. Jung, "Amorphous Pd-assisted H2 detection of ZnO nanorod gas sensor with enhanced sensitivity and stability," *Sensors and Actuators B: Chemical,* vol. 262, pp. 460-468, 2018.

[20] Z. Li *et al.*, "Room-Temperature High-Performance H2S Sensor Based on Porous CuO Nanosheets Prepared by Hydrothermal Method," *ACS applied materials & interfaces,* vol. 8, no. 32, pp. 20962-20968, 2016.

[21] S. M. Sievert, R. P. Kiene, and H. N. Schulz-Vogt, "The sulfur cycle," *Oceanography,* vol. 20, no. 2, pp. 117-123, 2007.

[22] A. Bassani *et al.*, "H2S in geothermal power plants: from waste to additional resource for energy and environment," 2018.

[23] F. Peng *et al.*, "Ultrasensitive ppb-level H2S gas sensor at room temperature based on WO3/rGO hybrids," *Journal of materials science. Materials in electronics,* vol. 31, no. 6, pp. 5008-5016, 2020.

[24] O. A. Habeeb, R. Kanthasamy, G. A. Ali, S. Sethupathi, and R. B. M. Yunus, "Hydrogen sulfide emission sources, regulations, and removal techniques: a review," *Reviews in Chemical Engineering,* vol. 34, no. 6, pp. 837-854, 2018.

[25] E.-L. S. Hinckley, J. T. Crawford, H. Fakhraei, and C. T. Driscoll, "A shift in sulfur-cycle manipulation from atmospheric emissions to agricultural additions," *Nature Geoscience,* vol. 13, no. 9, pp. 597-604, 2020.

[26] S. Rubright, "Cyanide and hydrogen sulfide: A review of two blood gases, their environmental sources, and potential risks," University of Pittsburgh, 2017.

[27] C.-H. Chou *et al.*, "Toxicological profile for hydrogen sulfide and carbonyl sulfide," 2016.

[28] S. L. M. Rubright, L. L. Pearce, and J. Peterson, "Environmental toxicology of hydrogen sulfide," *Nitric oxide: biology and chemistry,* vol. 71, p. 1, 2017.

[29] A. Gupta, S. Ibrahim, and A. Al Shoaibi, "Advances in sulfur chemistry for treatment of acid gases," *Progress in Energy and Combustion Science,* vol. 54, pp. 65-92, 2016.

[30] D. Li *et al.*, "High humidity enhanced surface acoustic wave (SAW) H2S sensors based on sol–gel CuO films," *Sensors and Actuators B: Chemical,* vol. 294, pp. 55-61, 2019.

[31] Y. Zhang *et al.*, "Optical H2S and SO2 sensor based on chemical conversion and partition differential optical absorption spectroscopy," *Spectrochimica Acta Part A: Molecular and Biomolecular Spectroscopy,* vol. 210, pp. 120-125, 2019.

[32] Z. Awang, "Gas sensors: A review," *Sens. Transducers,* vol. 168, no. 4, pp. 61-75, 2014.

[33] H. Nazemi, A. Joseph, J. Park, and A. Emadi, "Advanced micro-and nano-gas sensor technology: A review," *Sensors,* vol. 19, no. 6, p. 1285, 2019.

[34] A. O. Dikovska, P. A. Atanasov, S. Tonchev, J. Ferreira, and L. Escoubas, "Periodically structured ZnO thin films for optical gas sensor application," *Sensors and Actuators A: Physical,* vol. 140, no. 1, pp. 19-23, 2007.

[35] J. Hodgkinson and R. P. Tatam, "Optical gas sensing: a review," *Measurement Science and Technology,* vol. 24, no. 1, p. 012004, 2012.

[36] B. Renganathan, D. Sastikumar, G. Gobi, N. R. Yogamalar, and A. C. Bose, "Nanocrystalline ZnO coated fiber optic sensor for ammonia gas detection," *optics & laser technology,* vol. 43, no. 8, pp. 1398-1404, 2011.

[37] B. Renganathan, D. Sastikumar, R. Srinivasan, and A. Ganesan, "Nanocrystalline samarium oxide coated fiber optic gas sensor," *Materials Science and Engineering: B,* vol. 186, pp. 122-127, 2014.

[38] B. Renganathan and A. Ganesan, "Fiber optic gas sensor with nanocrystalline ZnO," *Optical Fiber Technology,* vol. 20, no. 1, pp. 48-52, 2014.

[39] S. Agarwal *et al.*, "Gas sensing properties of ZnO nanostructures (flowers/rods) synthesized by hydrothermal method," *Sensors and Actuators B: Chemical,* vol. 292, pp. 24-31, 2019.

[40] P. Cao *et al.*, "Ethanol sensing behavior of Pd-nanoparticles decorated ZnO-nanorod based chemiresistive gas sensors," *Sensors and Actuators B: Chemical,* vol. 298, p. 126850, 2019.

[41] J. H. Bang *et al.*, "Porous Si/SnO2 nanowires heterostructures for H2S gas sensing," *Ceramics international,* vol. 46, no. 1, pp. 604-611, 2020.

[42] V. Bochenkov and G. Sergeev, "Sensitivity, selectivity, and stability of gas-sensitive metal-oxide nanostructures," *Metal oxide nanostructures and their applications,* vol. 3, pp. 31-52, 2010.

[43] J.-H. Choi, H. Kim, H.-K. Sung, and H.-Y. Cha, "Investigation of Stability and Power Consumption of an AlGaN/GaN Heterostructure Hydrogen Gas Sensor Using Different Bias Conditions," *Sensors,* vol. 19, no. 24, p. 5549, 2019.

[44] Z. Hosseini and A. Mortezaali, "Room temperature H2S gas sensor based on rather aligned ZnO nanorods with flower-like structures," *Sensors and Actuators B: Chemical,* vol. 207, pp. 865-871, 2015.

[45] N. S. Ramgir *et al.*, "Room temperature H2S sensor based on Au modified ZnO nanowires," *Sensors and Actuators B: Chemical,* vol. 186, pp. 718-726, 2013.

[46] W. Yu *et al.*, "CuO/WO3 Hybrid Nanocubes for High-Responsivity and Fast-Recovery H2S Sensors Operated at Low Temperature," *Particle & Particle Systems Characterization,* vol. 33, no. 1, pp. 15-20, 2016.

[47] T. M. Salama, M. Morsy, R. M. Abou Shahba, S. H. Mohamed, and M. M. Mohamed, "Synthesis of Graphene Oxide Interspersed in Hexagonal WO3 Nanorods for High-

Efficiency Visible-Light Driven Photocatalysis and NH3 Gas Sensing," *Frontiers in chemistry,* vol. 7, pp. 722-722, 2019.

[48] S. Goel and B. Kumar, "A review on piezo-/ferro-electric properties of morphologically diverse ZnO nanostructures," *Journal of Alloys and Compounds,* p. 152491, 2019.

[49] K. Verma, D. K. Bharti, S. Badatya, A. K. Srivastava, and M. K. Gupta, "A high performance flexible two dimensional vertically aligned ZnO nanodisc based piezoelectric nanogenerator via surface passivation," *Nanoscale Advances,* vol. 2, no. 5, pp. 2044-2051, 2020.

[50] H. Li *et al.*, "Triboelectric-polarization-enhanced high sensitive ZnO UV sensor," *Nano Today,* vol. 33, p. 100873, 2020.

[51] R. W. Crisp *et al.*, "Atomic Layer Deposition of ZnO on InP Quantum Dot Films for Charge Separation, Stabilization, and Solar Cell Formation," *Advanced Materials Interfaces,* vol. 7, no. 4, p. 1901600, 2020.

[52] A. D. Ugale *et al.*, "ZnO decorated flexible and strong graphene fibers for sensing NO2 and H2S at room temperature," *Sensors and Actuators B: Chemical,* vol. 308, p. 127690, 2020.

[53] A. R. Nimbalkar and M. G. Patil, "Synthesis of ZnO thin film by sol-gel spin coating technique for H2S gas sensing application," *Physica B: Condensed Matter,* vol. 527, pp. 7-15, 2017.

[54] M. Wang, Q. Luo, S. Hussain, G. Liu, G. Qiao, and E. J. Kim, "Sharply-precipitated spherical assembly of ZnO nanosheets for low temperature H2S gas sensing performances," *Materials Science in Semiconductor Processing,* vol. 100, pp. 283-289, 2019.

[55] S. Shinde, G. Patil, D. Kajale, V. Gaikwad, and G. Jain, "Synthesis of ZnO nanorods by spray pyrolysis for H2S gas sensor," *Journal of Alloys and Compounds,* vol. 528, pp. 109-114, 2012.

[56] A. Yu, Z. Li, and J. Yi, "Selective detection of parts-per-billion H2S with Pt-decorated ZnO nanorods," *Sensors and Actuators B: Chemical,* vol. 333, p. 129545, 2021.

[57] Q. Li *et al.*, "Highly sensitive sensor based on ordered porous ZnO nanosheets for ethanol detecting application," *Sensors and Actuators B: Chemical,* vol. 326, p. 128952, 2021.

[58] N. Zhang, K. Yu, Q. Li, Z. Zhu, and Q. Wan, "Room-temperature high-sensitivity H 2 S gas sensor based on dendritic ZnO nanostructures with macroscale in appearance," *Journal of Applied Physics,* vol. 103, no. 10, p. 104305, 2008.

[59] M. Maruthupandy *et al.*, "Synthesis of metal oxide nanoparticles (CuO and ZnO NPs) via biological template and their optical sensor applications," *Applied Surface Science,* vol. 397, pp. 167-174, 2017.

[60] R. Tan *et al.*, "Enhanced open-circuit photovoltage and charge collection realized in pearl-like NiO/CuO composite nanowires based p-type dye sensitized solar cells," *Materials Research Bulletin,* vol. 116, pp. 131-136, 2019.

[61] S. Yang, P. Liu, Y. Wang, Z. Guo, R. Tan, and L. Qu, "Electrochemical sensor using poly-(l-cysteine) functionalized CuO nanoneedles/N-doped reduced graphene oxide for detection of lead ions," *RSC Advances,* vol. 10, no. 31, pp. 18526-18532, 2020.

[62] Q. Lei, H. Li, H. Zhang, J. Wang, W. Fan, and L. Cai, "Three-dimensional hierarchical CuO gas sensor modified by Au nanoparticles," *Journal of Semiconductors,* vol. 40, no. 2, p. 022101, 2019.

[63] Y. M. Choi *et al.*, "Ultrasensitive detection of VOCs using a high-resolution CuO/Cu2O/Ag nanopattern sensor," *Advanced Functional Materials,* vol. 29, no. 9, p. 1808319, 2019.

[64] Z. Li, Y. Liu, D. Guo, J. Guo, and Y. Su, "Room-temperature synthesis of CuO/reduced graphene oxide nanohybrids for high-performance NO2 gas sensor," *Sensors and Actuators B: Chemical,* vol. 271, pp. 306-310, 2018.

[65] S. Li *et al.*, "Metal-Organic frameworks-derived bamboo-like CuO/In2O3 Heterostructure for high-performance H2S gas sensor with Low operating temperature," *Sensors and Actuators B: Chemical,* vol. 310, p. 127828, 2020.

[66] K. Wu and C. Zhang, "Facile synthesis and ppb-level H 2 S sensing performance of hierarchical CuO microflowers assembled with nano-spindles," *Journal of Materials Science: Materials in Electronics,* pp. 1-9, 2020.

[67] K. Santra, C. Sarkar, M. Mukherjee, and B. Ghosh, "Copper oxide thin films grown by plasma evaporation method," *Thin Solid Films,* vol. 213, no. 2, pp. 226-229, 1992.

[68] Z. Li *et al.*, "Hydrothermal synthesis of hierarchically flower-like CuO nanostructures with porous nanosheets for excellent H2S sensing," *Journal of Alloys and Compounds,* vol. 725, pp. 1136-1143, 2017.

[69] X. Wen, W. Zhang, S. Yang, Z. R. Dai, and Z. L. Wang, "Solution phase synthesis of Cu (OH) 2 nanoribbons by coordination self-assembly using Cu2S nanowires as precursors," *Nano Letters,* vol. 2, no. 12, pp. 1397-1401, 2002.

[70] X. Wang *et al.*, "Preparation of In2O3 Thin Film and The Study of Gas Sensitivity to Ethanol," *Integrated Ferroelectrics,* vol. 199, no. 1, pp. 58-68, 2019.

[71] Y. Shen *et al.*, "In-situ growth of mesoporous In2O3 nanorod arrays on a porous ceramic substrate for ppb-level NO2 detection at room temperature," *Applied Surface Science,* vol. 498, p. 143873, 2019.

[72] D. Zhang *et al.*, "Detection of NO2 down to ppb levels using individual and multiple In2O3 nanowire devices," *Nano letters,* vol. 4, no. 10, pp. 1919-1924, 2004.

[73] W. Liu, Y. Xie, T. Chen, Q. Lu, S. U. Rehman, and L. Zhu, "Rationally designed mesoporous In2O3 nanofibers functionalized Pt catalysts for high-performance acetone gas sensors," *Sensors and Actuators B: Chemical,* vol. 298, p. 126871, 2019.

[74] Z. Li *et al.*, "Hydrogen gas sensor based on mesoporous In2O3 with fast response/recovery and ppb level detection limit," *International Journal of Hydrogen Energy,* vol. 43, no. 50, pp. 22746-22755, 2018.

[75] D. Han, L. Zhai, F. Gu, and Z. Wang, "Highly sensitive NO2 gas sensor of ppb-level detection based on In2O3 nanobricks at low temperature," *Sensors and Actuators B: Chemical,* vol. 262, pp. 655-663, 2018.

[76] S. K. Lim, S.-H. Hwang, D. Chang, and S. Kim, "Preparation of mesoporous In2O3 nanofibers by electrospinning and their application as a CO gas sensor," *Sensors and Actuators B: Chemical,* vol. 149, no. 1, pp. 28-33, 2010.

[77] K. Anand, J. Kaur, R. C. Singh, and R. Thangaraj, "Preparation and characterization of Ag-doped In2O3 nanoparticles gas sensor," *Chemical Physics Letters,* vol. 682, pp. 140-146, 2017.

[78] R. H. Bari, P. P. Patil, S. B. Patil, and A. R. Bari, "Detection of H 2 S gas at lower operating temperature using sprayed nanostructured In 2 O 3 thin films," *Bulletin of Materials Science,* vol. 36, no. 6, pp. 967-972, 2013.

[79] Y. Wang *et al.*, "Room temperature H2S gas sensing properties of In2O3 micro/nanostructured porous thin film and hydrolyzation-induced enhanced sensing mechanism," *Sensors and Actuators B: Chemical,* vol. 228, pp. 74-84, 2016.

[80] L. Xu, B. Dong, Y. Wang, X. Bai, Q. Liu, and H. Song, "Electrospinning preparation and room temperature gas sensing properties of porous In2O3 nanotubes and nanowires," *Sensors and Actuators B: Chemical,* vol. 147, no. 2, pp. 531-538, 2010.

[81] H. Duan *et al.*, "The fabrication of In2O3 toruloid nanotubes and their room temperature gas sensing properties for H2S," *Materials Research Express,* vol. 4, no. 9, p. 095022, 2017.

[82] M. Kaur *et al.*, "Room-temperature H2S gas sensing at ppb level by single crystal In2O3 whiskers," *Sensors and Actuators B: Chemical,* vol. 133, no. 2, pp. 456-461, 2008.

[83] C. Karthikeyan, P. Arunachalam, K. Ramachandran, A. M. Al-Mayouf, and S. Karuppuchamy, "Recent advances in semiconductor metal oxides with enhanced methods for solar photocatalytic applications," *Journal of Alloys and Compounds,* vol. 828, p. 154281, 2020.

[84] A. Mehmood, X. Long, A. A. Haidry, and X. Zhang, "Trends in sputter deposited tungsten oxide structures for electrochromic applications: A review," *Ceramics International,* 2020.

[85] C. A. Bignozzi, S. Caramori, V. Cristino, R. Argazzi, L. Meda, and A. Tacca, "Nanostructured photoelectrodes based on WO 3: applications to photooxidation of aqueous electrolytes," *Chemical Society Reviews,* vol. 42, no. 6, pp. 2228-2246, 2013.

[86] Z.-X. Cai, H.-Y. Li, J.-C. Ding, and X. Guo, "Hierarchical flowerlike WO3 nanostructures assembled by porous nanoflakes for enhanced NO gas sensing," *Sensors and Actuators B: Chemical,* vol. 246, pp. 225-234, 2017.

[87] M. Wang *et al.*, "WO3 porous nanosheet arrays with enhanced low temperature NO2 gas sensing performance," *Sensors and Actuators B: Chemical,* p. 128050, 2020.

[88] C. M. Hung, N. Van Duy, V. Van Quang, N. Van Toan, N. Van Hieu, and N. D. Hoa, "Facile synthesis of ultrafine rGO/WO3 nanowire nanocomposites for highly sensitive toxic NH3 gas sensors," *Materials Research Bulletin,* vol. 125, p. 110810, 2020.

[89] T. Zhao *et al.*, "Confined interfacial micelle aggregating assembly of ordered macro–mesoporous tungsten oxides for H 2 S sensing," *Nanoscale,* vol. 12, no. 40, pp. 20811-20819, 2020.

[90] S. Poongodi *et al.*, "Electrodeposition of WO3 nanostructured thin films for electrochromic and H2S gas sensor applications," *Journal of Alloys and Compounds,* vol. 719, pp. 71-81, 2017.

[91] N. Kaur, D. Zappa, N. Poli, and E. Comini, "Integration of VLS-Grown WO3 Nanowires into Sensing Devices for the Detection of H2S and O3," *ACS omega,* vol. 4, no. 15, pp. 16336-16343, 2019.

[92] Y. Li *et al.*, "Highly ordered mesoporous tungsten oxides with a large pore size and crystalline framework for H2S sensing," *Angewandte Chemie,* vol. 126, no. 34, pp. 9181-9186, 2014.

[93] X. San, Y. Lu, G. Wang, D. Meng, X. Gong, and Q. Jin, "In situ growth of WO3 nanotube arrays and their H2S gas sensing properties for reduced operating temperature," *Materials Letters,* p. 127716, 2020.

[94] M. Paknahad, J. S. Bachhal, A. Ahmadi, and M. Hoorfar, "Characterization of channel coating and dimensions of microfluidic-based gas detectors," *Sensors and Actuators B: Chemical,* vol. 241, pp. 55-64, 2017.

[95] B. Inkson, "Scanning electron microscopy (SEM) and transmission electron microscopy (TEM) for materials characterization," in *Materials characterization using nondestructive evaluation (NDE) methods*: Elsevier, 2016, pp. 17-43.

[96] F. A. Stevie and C. L. Donley, "Introduction to x-ray photoelectron spectroscopy," *Journal of Vacuum Science & Technology A: Vacuum, Surfaces, and Films,* vol. 38, no. 6, p. 063204, 2020.

[97] M. Yin, M. Liu, and S. Liu, "Diameter regulated ZnO nanorod synthesis and its application in gas sensor optimization," *Journal of alloys and compounds,* vol. 586, pp. 436-440, 2014.

[98] R. Gao *et al.*, "Highly selective detection of saturated vapors of abused drugs by ZnO nanorod bundles gas sensor," *Applied Surface Science,* vol. 485, pp. 266-273, 2019.

[99] S. Shaikh, V. Ganbavale, S. Mohite, U. Patil, and K. Rajpure, "ZnO nanorod based highly selective visible blind ultra-violet photodetector and highly sensitive NO2 gas sensor," *Superlattices and Microstructures,* vol. 120, pp. 170-186, 2018.

[100] Z. Liu, T. Fan, D. Zhang, X. Gong, and J. Xu, "Hierarchically porous ZnO with high sensitivity and selectivity to H2S derived from biotemplates," *Sensors and Actuators B: Chemical,* vol. 136, no. 2, pp. 499-509, 2009.

[101] G. S. Aluri *et al.*, "Highly selective GaN-nanowire/TiO2-nanocluster hybrid sensors for detection of benzene and related environment pollutants," *Nanotechnology,* vol. 22, no. 29, p. 295503, 2011.

[102] Z. Wen and L. Tian-Mo, "Gas-sensing properties of SnO2–TiO2-based sensor for volatile organic compound gas and its sensing mechanism," *Physica B: Condensed Matter,* vol. 405, no. 5, pp. 1345-1348, 2010.

[103] N. Barsan and U. Weimar, "Conduction model of metal oxide gas sensors," *Journal of electroceramics,* vol. 7, no. 3, pp. 143-167, 2001.

[104] J. M. Walker, S. A. Akbar, and P. A. Morris, "Synergistic effects in gas sensing semiconducting oxide nano-heterostructures: A review," *Sensors and actuators. B, Chemical,* vol. 286, pp. 624-640, 2019.

[105] W. Zang, Y. Nie, D. Zhu, P. Deng, L. Xing, and X. Xue, "Core–shell In2O3/ZnO nanoarray nanogenerator as a self-powered active gas sensor with high H2S sensitivity

and selectivity at room temperature," *The Journal of Physical Chemistry C,* vol. 118, no. 17, pp. 9209-9216, 2014.

[106] C. Li, Z. Du, L. Li, H. Yu, Q. Wan, and T. Wang, "Surface-depletion controlled gas sensing of ZnO nanorods grown at room temperature," *Applied Physics Letters,* vol. 91, no. 3, p. 032101, 2007.

[107] G. Korotcenkov, "The role of morphology and crystallographic structure of metal oxides in response of conductometric-type gas sensors," *Materials Science and Engineering: R: Reports,* vol. 61, no. 1-6, pp. 1-39, 2008.

[108] J. M. Walker, S. A. Akbar, and P. A. Morris, "Synergistic effects in gas sensing semiconducting oxide nano-heterostructures: A review," *Sensors and Actuators B: Chemical,* vol. 286, pp. 624-640, 2019.

[109] S. Nundy, T.-y. Eom, K.-Y. Song, J.-S. Park, and H.-J. Lee, "Hydrothermal synthesis of mesoporous ZnO microspheres as NOX gas sensor materials—Calcination effects on microstructure and sensing performance," *Ceramics International,* vol. 46, no. 11, pp. 19354-19364, 2020.